MINIREVIEW

Check for updates

Two-dimensional ferroelectric synaptic devices enabled by diverse coupling mechanisms

Youna Huang, [ID] [a,b,c] Wei Wang, [ID] [b] Yang Li [ID] [b] and Changjian Li [ID] *[a,c]

Two-dimensional (2D) van der Waals (vdW) ferroelectric (FE) materials have recently emerged as promising candidates for advanced synaptic devices in brain-inspired neuromorphic computing systems. These materials retain ferroelectricity down to a few atomic layers, including the monolayer limit. Their unique properties—such as atomically clean surface/interface, mechanical flexibility, and LEGO®-like stacking capability—offer significant advantages for complementary metal−oxide-semiconductor (CMOS)-compatible fabrication, enabling high integration density, energy-efficient operation, and fast switching speed. Importantly, the intrinsic polarization in 2D ferroelectrics can couple with various physical phenomena, enabling the emulation of complex biological synaptic behaviors. This review provides a comprehensive overview of recent advances in 2D ferroelectric-based synaptic devices, with a particular focus on the role of coupling mechanisms within these materials. Firstly, we introduce the principles of neuromorphic computing, and advantages of 2D ferroelectric materials. Next, we classify 2D ferroelectric materials according to five key types of coupling mechanisms. We then review representative studies on 2D FE-based synaptic devices by analyzing how each coupling mechanism is utilized to achieve synaptic functionality. Finally, we discuss current challenges and prospects for leveraging these coupling mechanisms in synaptic applications. The purpose of this review is to provide a structured understanding of how intrinsic coupling in 2D ferroelectric materials can be utilized for the design of high-performance and biologically inspired synaptic devices.

1. Introduction

The von Neumann architecture,[1] which dominates modern computing, separates the central processing unit (CPU) from memory, resulting in the *memory wall* bottleneck characterized by high latency, large area overhead, and significant energy consumption. These limitations severely hinder the performance of data-intensive applications such as artificial intelligence (AI) and the Internet of Things (IoT),[2–6] with tasks like training a neural architecture search model on a GPU consuming up to 650 000 kWh of energy.[7] Overcoming this challenge requires new computing paradigms that reduce data movement and improve energy efficiency.

Neuromorphic computing seeks to emulate the architecture and functional principles of the human brain—spanning sensing, processing, and learning—by transmitting and processing only the changes in information, analogous to neural

spikes in biological systems. As an inherently event- or data-driven paradigm, it enables ultra-low power operation. Fully CMOS-based neuromorphic hardware,[8–10] such as IBM TrueNorth,[11] Intel Loihi,[12] Tianjic,[13] and ODIN,[14] has demonstrated the feasibility of this approach by implementing neuron and synapse functionalities with CMOS transistors, capacitors, and SRAM-based circuits.[15,16] For instance, Loihi has achieved adaptive robotic arm control with 40x lower energy consumption and 50% faster processing compared to GPU.[17] However, the scalability of CMOS-based neuromorphic hardware is hindered by circuit complexity and area cost. In contrast, non-volatile memory (NVM) technologies—such as resistive random-access memory (RRAM), phase-change memory (PCM), ferroelectric memory (FeRAM) and transistors (FeFET), and magnetoresistive RAM (MRAM)—offer high integration density, low programming energy, and multilevel conductance capabilities, making them promising candidates for next-generation neuromorphic chips.

In parallel, emerging memristive devices based on functional materials—including two-dimensional (2D) materials, perovskites, and organic polymers—exhibit desirable features such as high-density array compatibility, fast switching speeds, and the ability to emulate biological synapses through direct mapping of synaptic weight to device conductance.[18,19]

[a]*Department of Materials Science and Engineering, Southern University of Science and Technology, Shenzhen, Guangdong 518105, China. E-mail: licj@sustech.edu.cn*
[b]*Pengcheng Laboratory, Shenzhen 518000, Guangdong, China*
[c]*Guangdong Provincial Key Laboratory of Functional Oxide Materials and Devices, Southern University of Science and Technology, Shenzhen, Guangdong, 518055, China*

Although current demonstrations are largely limited to individual devices or small-scale arrays, and often remain at the simulation level, these technologies hold substantial promise. To bridge the gap between laboratory research and practical circuit-level integration, it is essential to further explore their working mechanisms and intrinsic properties.

1.1 Characteristics of biological synapses and neurons

Biological neural networks in the human brain consist of approximately 10^{11} neurons and 10^{15} synapses, enabling the efficient processing of vast amounts of information with extremely low power consumption (around 20 W).[20–23] Each synaptic event consumes as little as 10 femtojoules (fJ) of energy.[24] Within a biological neural system, a neuron receives the excitatory or inhibitory postsynaptic current (EPSC or IPSC) through its dendrites. These electrical signals are integrated in the cell body, leading to changes in the membrane potential. When this potential reaches a certain threshold, it triggers the generation of an action potential, or an output spike, following the leaky integrated fire (LIF) model.[25–27] This action potential propagates to the axon terminals (pre-synapse), where the opening of calcium ion (Ca^{2+}) channel allows Ca^{2+} to enter. This influx triggers vesicle fusion with cell membranes, releasing neurotransmitters into the synaptic gap.[28] Following neurotransmitter release, the neuron returns to its initial state (resting state). The collective dynamics of neuronal populations give rise to higher-order functions such as pattern recognition and decision-making.

Synaptic weight—representing the strength of the connection between pre- and post-synaptic neuron—plays a central role in memory and learning, with synaptic plasticity referring to the modulation of these weights. Two key forms of plasticity are short-term plasticity (STP) and long-term plasticity (LTP), which differ primarily in duration (retention time) of synaptic weight. STP, lasting from milliseconds to minutes, is involved in temporal computational processes, while LTP, which lasts for hours or more, plays a central role in memory and learning.[29] The transition from STP to LTP is essential for implementing memory and forgetting mechanisms.

STP includes paired-pulse facilitation (PPF) and paired-pulse depression (PPD), while LTP encompasses spike-timing-dependent plasticity (STDP), spike-rate-dependent plasticity (SRDP), and spike-amplitude-dependent plasticity (SADP).[30,31] Each mechanism involves two directions of synaptic weight regulation: potentiation and depression. Both PPF/PPD and STDP are triggered by two identical pulses with a specific time interval (ΔT). In PPF and PPD, paired pulses are applied to the pre-synapse, whereas in STDP, SRDP, and SADP, one pulse is supplied to the pre-synaptic neurons and the other to the post-synaptic neuron. PPF and PPD demonstrate that a reduced or increased interval between paired pulses results in an increased or decreased postsynaptic current, respectively, triggered by the second pulse. Conversely, in STDP, when the pre-synaptic spike precedes the post-synaptic spike ($\Delta T > 0$), the synaptic connection strength is enhanced, with the degree of potentiation increasing as the interval shortens. When the

post-synaptic spike occurs before the pre-synaptic spike ($\Delta T < 0$), the synaptic strength is typically suppressed.[23,32] This phenomenon is consistent with the Hebbian learning rule.[33] The SRDP is characterized by a train of identical pulses, where the synaptic strength is enhanced when the rate of the pulse train is high and is weakened when the rate is low. In SADP, a single pulse modulates synaptic strength depending on its amplitude. Furthermore, the decay behavior of PPF can be described by the equation:

$$\text{PPF} = c_1 \exp\left(-\frac{\Delta T}{\tau_1}\right) + c_2 \exp\left(-\frac{\Delta T}{\tau_2}\right)$$

where ΔT is the pulse interval, c_1 and c_2 are facilitation magnitudes, and τ_1, τ_2 are the characteristic relaxation times of the rapid and slow decay phases, respectively. For artificial synaptic devices to emulate biological behavior accurately, their time constants must be on the same order of magnitude, typically ranging from milliseconds to seconds.[34]

The behavior of individual neurons and synapses forms the foundation of the collective of neural computation, enabling powerful system-level functions such as learning, pattern recognition, and memory formation.[18] Recent advances have increasingly focused on replicating these biological neuronal and synaptic behaviors in artificial devices, as accurate emulation of biological plasticity is essential for functional neuromorphic systems.[35–42] These systems offer unique advantages over conventional von Neumann architectures, including massive parallelism, high energy efficiency, and adaptive learning, making neuromorphic computing a compelling solution to current computational bottlenecks.[43]

The fundamental performance requirements for artificial synapses—which rely on direct mapping between synaptic weight and device conductance—include analog resistance modulation, controllable synaptic weight adjustment, and support for practical synaptic plasticity.[31] Key evaluation metrics such as memory window, switching ratio, endurance, retention, programming speed, and the number of conductance states are critical for emulating biological synaptic behavior and meeting stringent demands on energy efficiency, scalability, and hardware integration (Fig. 1). For instance, **endurance** refers to the number of write cycles a device can sustain without significant degradation (typically larger than 10^9 cycles),[44] while **retention** reflects the duration over which a conductance state remains stable without relaxation, both of which are vital for reliable data storage in computation-intensive applications. **Programming speed**, or latency, is also crucial—devices should ideally support sub-microsecond or nanosecond-level switching to enable real-time signal processing and high-speed learning.[45] Furthermore, artificial synapses should offer multiple stable and clearly distinguishable conductance states, with minimal overlap and strong retention, to ensure precise weight updates and enhanced learning resolution. Energy efficiency is another important metric. State-of-the-art devices aim for energy consumption below the picojoule (pJ) level per synaptic event, approaching or surpassing that of biological synapses (about 10
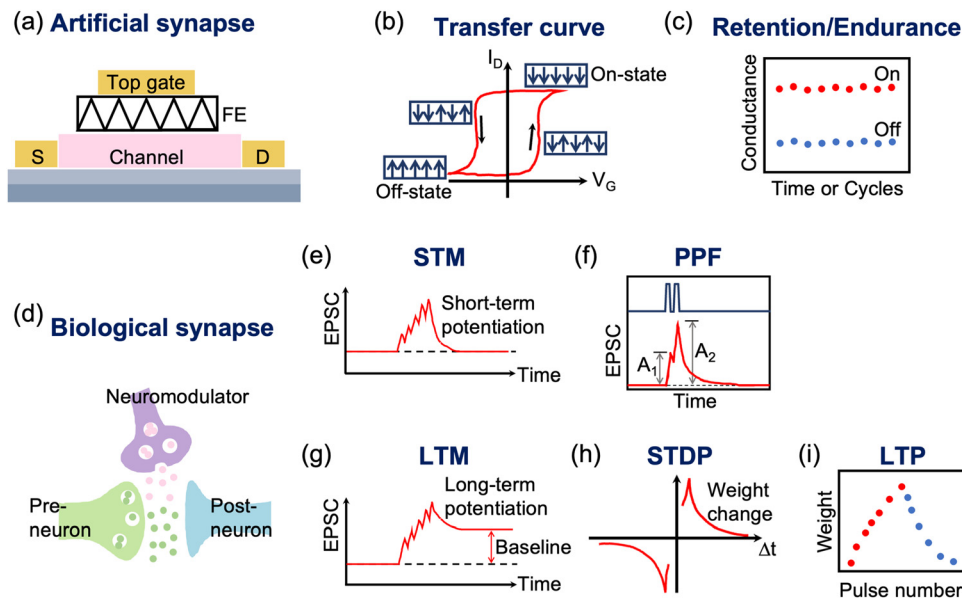
Fig. 1 Biological and artificial synaptic signal processing. (a) Schematic illustration of an FeFET-based artificial synapse. (b) Typical transfer curve of an FeFET-based memory device. (c) Representative retention and endurance characteristics of FeFET. (d) Schematic of a biological synapse. (e) Short-term potentiation (STP). (g) long-term potentiation (LTP). (f) PPF operation by two input pulses with a certain time interval; the upper panel shows the input voltage, and the lower panel shows the corresponding postsynaptic current (PSC). (h) STDP implementation. (i) Synaptic weight modulation curve showing LTP and LTD.

femtojoules).[44,46] In addition, gradual, symmetric, and linear conductance modulation in response to pre- and post-synaptic spikes or external stimuli is essential—high linearity facilitates accurate training, and symmetry between potentiation and depression minimizes cumulative learning errors. For large-scale neuromorphic architectures such as crossbar arrays, minimizing **device-to-device (D2D)** and **cycle-to-cycle (C2C) variability**, while ensuring integration compatibility and scalability, is crucial for achieving reproducible learning behavior and manufacturability. Lastly, in artificial neurons, volatile memristors can emulate **leaky integrate-and-fire (LIF)** behavior, where the primary benchmark is the neuron's ability to accumulate stimuli during input pulse trains and subsequently reset after stimulation ceases.

1.2 Ferroelectric materials for neuromorphic computing

Ferroelectrics are characterized by the presence of stable and switchable spontaneous polarization (P_s), which can be reversed under an external electric field exceeding the coercive field. This spontaneous polarization arises in the absence of an applied voltage and originates from the non-coincidence between the centers of positive and negative charges within the crystal lattice. Macroscopically, P_s represents the net electric dipole moment per unit volume. The emergence of ferroelectricity is inherently linked to symmetry breaking in the crystal structure.

The phenomenon of ferroelectricity was first discovered by Valasek in 1921[47] in Rochelle salt—[$KNa(C_4H_4O_6) \cdot 4H_2O$], an organic molecular crystal—thus formally establishing the concept of ferroelectricity. However, the material's water solubi-

lity and mechanical brittleness hindered its practical applications. A major breakthrough came in the 1950s with the successful deposition of robust thin films of three-dimensional (3D) perovskite oxides ferroelectrics, such as barium titanate ($BaTiO_3$, BTO) and lead zirconate titanate ($Pb[Zr_xTi_{1-x}O_3]$, PZT).[48,49] These materials remain among the most representative 3D ferroelectrics, with applications in ferroelectric random-access memory (FeRAM), microelectromechanical systems (MEMS), and ferroelectric photovoltaics.[50–52] In recent years, doped hafnium oxide (HfO_2)[53–55] and scandium nitride (AlScN)[56,57] thin films have emerged as promising candidates for modern ferroelectric devices due to their excellent ferroelectric properties and compatibility with complementary metal–oxide-semiconductor (CMOS) technologies.[57,58] These materials enable the development of highly integrated ferroelectric components.

The ability of ferroelectric materials to maintain permanent electrical polarization below certain critical temperatures makes them well-suited as synaptic weight elements for information storage and artificial synapses.[46,55,59–61] Moreover, ferroelectric materials support multilevel polarization states, which can be achieved through partial polarization reversal using electrical pulses.[62] When integrated with semiconductor materials, polarization-controlled resistance modulation enables the emulation of synaptic plasticity observed in biological systems. For example, researchers have fabricated ferroelectric synaptic transistors using 3D ferroelectric polymers such as P(VDF-TrFE), which not only emulate synaptic behavior but also support in-memory sensing and logic processing.[38,41,63–65] Additionally, Du *et al.* demonstrated a neuromorphic visual sensing application by integrating a BTO

ferroelectric film with monolayer MoS_2 to fabricate ferroelectric phototransistors.[51]

However, as the demand for miniaturization and on-chip integration increases in nanoelectronics, conventional bulk ferroelectrics face intrinsic limitations at reduced thicknesses. This include the emergence of strong depolarization fields and structural instabilities, due to surface reconstruction and dangling bonds.[66] The depolarization field arises from unscreened polarization bound charges at the interfaces, generating an internal electric field opposite to the polarization direction—its strength increases as film thickness decreases. Moreover, when the thickness drops below a critical value, spontaneous polarization may vanish due to diminished long-range Coulomb interactions, enhanced depolarizing fields, and surface reconstruction. These limits have redirected research efforts toward low-dimensional ferroelectric materials, which exhibit robust polarization behavior down to the atomic limit and hold promise for next generation nanoelectronics and neuromorphic applications.

1.3 2D Ferroelectric materials for neuromorphic computing

Intrinsic two-dimensional (2D) van der Waals (vdW) materials, with nearly atomic thickness, offer promising solutions to modern technological challenges and serve as a foundation for next-generation nanoscale devices.[67–72] Since the discovery of graphene, 2D materials have attracted extensive research attention due to their unique electrical properties, including charge and thermal transport confined to a single atomic plane, atomically smooth surfaces, and the absence of dangling bonds.[67,73] These properties result in ideal periodic arrangement and uniform charge distribution. Representative 2D material include graphene, black phosphorus, transition metal dichalcogenides (TMDCs), and others. Among these, 2D ferroelectric (FE) materials, such as $CuInP_2S_6$,[74–78,78–80] $CuCrP_2S_6$,[81–88] α-In_2Se_3,[89–94] Bi_2O_2Se,[95–100] SnX (X = S, Se, Te),[101–106] XTe_2(M = W, Mo),[37,107–111] retain intrinsic ferroelectricity down to the monolayer limit. Their dangling-bond-free vdW surfaces and compatibility with traditional semiconductor technologies make them highly promising for nano-electronic applications.[112,113]

Field-effect transistors (FETs) based on 2D materials have demonstrated the ability to emulate artificial synapse behavior using a simple structure, where the source and drain act as the pre- and post-synapse, and the gate functions as the neuromodulator.[114–116] For example, in 2017, a MoS_2 back-gate FET was used to emulate LTP behavior by leveraging the non-ideal threshold voltage and the slow response of interface charge traps.[117] A MoS_2-based crossbar array was also developed to regulate synaptic weights and applied in spiking neural networks (SNNs),[118,119] showing high accuracy, low energy consumption, and low operating voltage. In 2018, a WSe_2/graphene Schottky diode demonstrated essential synaptic properties—such as STM, LTP and PPF—enabled by electrostatically controlled modulation of the barrier height.[120] However, in 2D semiconductor materials, the realization of the memory and synaptic weight modulation often relies on intrinsic defects. These defects disrupt the periodic atomic structure of 2D materials and hinder

their ability to fully leverage their intrinsic advantages. Furthermore, device performance is significantly limited by the poor reliability and limited tunability of ion migration, which occurs at the atomic scale and is typically uncontrollable.

In contrast, 2D ferroelectric materials, as low-dimensional functional materials, are more promising candidates for synaptic weight modulation. Ferroelectric polarization facilitates non-volatile interfacial charge modulation, thereby enabling multi-level memory effects. Recently, various 2D ferroelectrics have been synthesized and applied in neuromorphic devices.[74,81,94,101,107,110,121] These devices often have different architectures and mechanisms, posing challenges for understanding their underlying mechanisms and designing the next-generation neuromorphic components. Unlike previous reviews[4,24,113,122–124] that are primarily organized by material classification or device architecture, this review focuses on the fundamental physical mechanism of 2D ferroelectric materials in synaptic applications. We highlight 2D ferroelectric-based synaptic devices with diverse functionalities and superior performance, enabled by the coupling between ferroelectric polarization and internal conductive morphology.

In this review, we provide an overview of recent advancements in memory and synaptic device applications utilizing 2D ferroelectric materials. We begin with a brief introduction to the fundamentals of ferroelectricity, followed by a discussion of intrinsic ferroelectric mechanisms and their distinct physical properties. Particular attention is given to ferroelectric coupling phenomena that arise at the material level, including (i) intrinsic polarization, (ii) polarization-ion migration coupling, (iii) polarization-carrier coupling and (iv) the interaction between out-of-plane (OOP) and in-plane (IP) polarization, and polarization coupling between two ferroelectrics, (v) polarization-light coupling (section 2). We then categorize recent developments in high-performance 2D ferroelectric-based neuromorphic devices according to how intra- and inter- material ferroelectric coupling mechanisms are employed to realize device functionalities. This classification results in five distinct categories: (i) ferroelectric (FE)-dominated, (ii) FE-ion migration coupled, (iii) FE-semiconductor coupled, (iv) FE-FE coupled, and (v) FE-light stimulation coupled devices (section 3). Finally, we conclude with a discussion on the current challenges and potential opportunities associated with these coupling mechanisms in both 2D ferroelectric materials and their device-level implementations (section 4). It is worth noting that section 2 focuses on polarization coupling mechanisms within the 2D ferroelectric materials themselves, which is why the term "polarization" is used. In contrast, section 3 discusses device-level implementations, where the term "ferroelectric" is more appropriate.

2. Coupling mechanisms in 2D ferroelectric materials

Table 1 is the summary of the fundamental physical properties of 2D ferroelectric materials, highlighting their intrinsic ferroelectric characteristics.

Table 1 Summary of 2D ferroelectric materials

Material	Ferroionic		Ferroelectric semiconductor		Ferroelectric superconductor		Ferroelectric metal
	$CuInP_2S_6$ (ref. 125)	$CuCrP_2S_6$ (ref. 126)	$\alpha\text{-}In_2Se_3$ (ref. 127)	Bi_2O_2Se (ref. 128)	SnS, SnTe (ref. 101)	$MoTe_2$ 300 K	WTe_2 (ref. 107)
Curie temperature	315 K (ref. 125)	390 K (ref. 126)	500 K (ref. 127)	508 K (ref. 128)	270 K (ref. 101)	300 K	350 K (ref. 107)
Spontaneous polarization	3.7 μC cm⁻² (ref. 129)	16.05 μC cm⁻² (ref. 83)	–	35 μC cm⁻² (ref. 97)	1.81 C m⁻¹ (ref. 130)	–	–
Limit thickness	4 nm (ref. 75)	2.6 nm (ref. 83)	1.2 nm (ref. 94)	6 nm (ref. 131)	–	0.8 nm	1.4 nm (ref. 107)
Band gap	2.9 eV (ref. 132)	1.22 eV (ref. 83)	1.3 eV (ref. 133)	2.09 eV (ref. 100) (monolayer)	1.1 eV (ref. 134)	1.1 eV (ref. 135)	–
Unique properties	Quadruple-well ferroelectricity (ref. 136)	Ferromagnetic, antiferromagnetic	Dipole-locking effect. Layer dependent ferroelectricity.	High mobility (ref. 99)	Purely in-plane ferroelectricity	–	Metallic ferroelectricity
Polarization	IP + OOP	OOP	IP + OOP	IP + OOP	IP	OOP	OOP
Polarization + ion	✓	✓	✗	✗	✗	✗	✗
Polarization + carrier	✗	✗	✓	✓	✓	✓	✓
Polarization coupling	✓	–	✓	–	✗	✗	✗
Polarization + light	✓	–	✓	✓	✓	✓	–

2.1 Polarization-only mechanism

Polarization in 2D ferroelectrics can be categorized into out-of-plane (OOP) and in-plane (IP) components. 2D ferroelectrics exhibit robust ferroelectricity down to just a few atomic layers at room temperature. Their van der Waals (vdW) bond-free surfaces facilitate seamless integration with other materials by eliminating lattice mismatch issues and minimizing charge trapping and interfacial oxide formation at ferroelectric/semiconductor interfaces. Based on their formation mechanisms, 2D ferroelectrics can be classified into two types: **intrinsic ferroelectrics**, which originate from non-centrosymmetric crystal structures, and **interlayer-sliding ferroelectrics**, where ferroelectricity results from interlayer slipping that breaks centrosymmetry and induces vertical polarization.[137–141]

This review mainly focuses on experimentally verified 2D ferroelectric materials, particularly van der Waals ferroelectrics such as $CuInP_2S_6$, $\alpha\text{-}In_2Se_3$, Bi_2O_2Se, SnTe, $MoTe_2$, WTe_2. Artificially engineered ferroelectrics[137–142] and single-element ferroelectrics[143] are excluded from the discussion.

2.2 Polarization-ion migration coupling mechanism

The polarization-ion migration coupling arises from the presence of mobile ions within certain 2D ferroelectric materials—such as Cu^+ ions in $CuInP_2S_6$ or $CuCrP_2S_6$, and selenium vacancies in $\alpha\text{-}In_2Se_3$ or Bi_2O_2Se. Although intrinsic ionic migration can introduce disorder that disrupts the long-range alignment of ferroelectric dipoles and consequently degrades polarization stability, it also offers functional advantages by mimicking the release and transport of neurotransmitter ions in synaptic processes.[28,43,98,144] When the interplay between ferroelectric polarization switching and ion migration is properly controlled, these materials can emulate various features of biological synapses, making polarization-ion coupled 2D ferroelectrics promising candidates for neuromorphic device applications.

2.2.1 $CuInP_2S_6$-based systems. Copper indium thiophosphate ($CuInP_2S_6$, CIPS), one of the van der Waals (vdW) ferroelectrics within the transition metal thio/seleno-phosphates (MTPS) family (chemical formula of $M_1M_2P_2X_6$),[83] has attracted great attention due to its unique structure and innovative properties, including low-dimensional ferroelectricity, ionic conductivity, tunable quadruple-potential wells characteristics,[136] negative piezoelectricity[79] and flexoelectric effect.[145,146] The polarization direction of CIPS can maintain for almost two months after being switched,[147] which is essential for achieving the non-volatile memory. CIPS demonstrates a broad band gap of 2.9 eV (ref. 76, 132 and 148) and a Curie temperature of 315 K.[78,125,148] The crystal structure of CIPS consists of an octahedral sulfur cage containing metal cations (Cu^+ and In^+), as well as phosphorus (P–P) pairs that occupy octahedral voids and form distinct triangular networks (Fig. 2a).[149]

The polarization-ionic coupling in CIPS stems from the movement of copper cations. There are three distinct crystallographic occupation sites for Cu ions: central octahedral Cu^1,
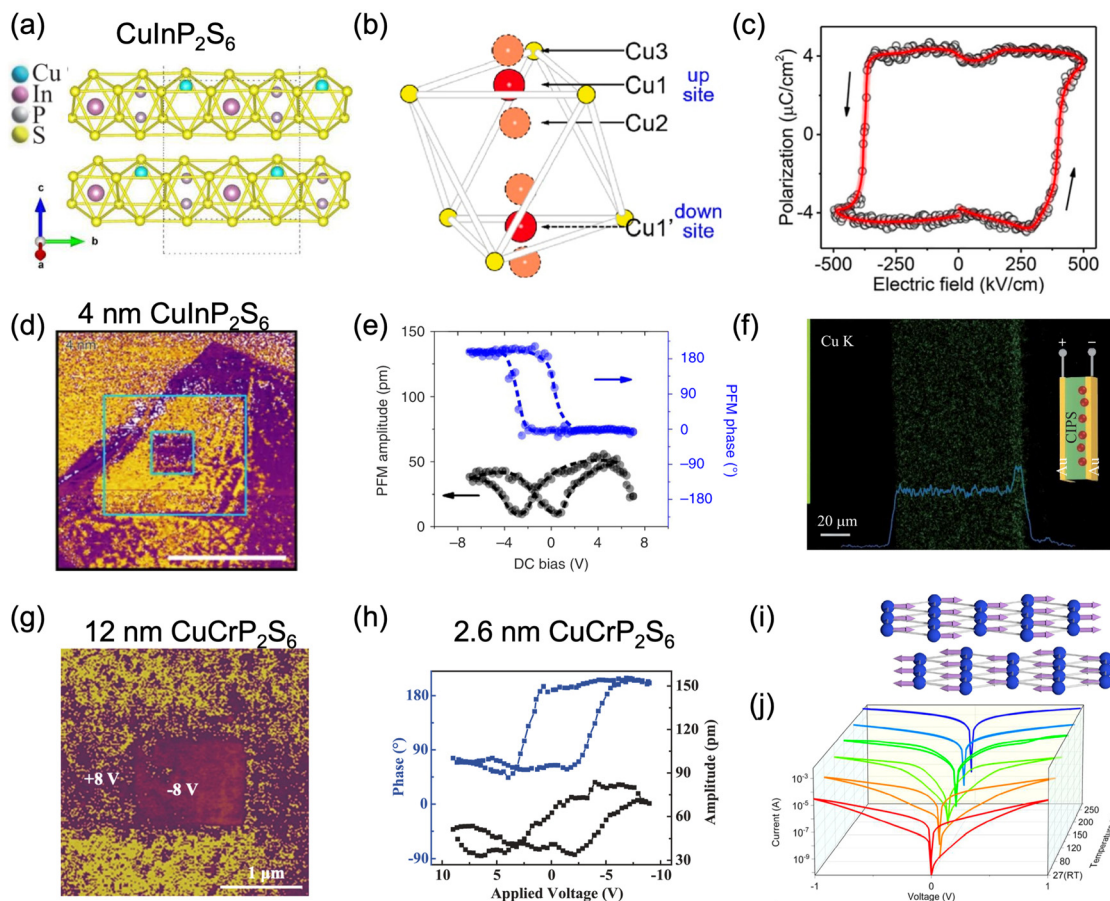
Fig. 2 Ferroelectric properties of $CuInP_2S_6$ (CIPS) and $CuCrP_2S_6$ (CCPS). (a) Crystal structure of $CuInP_2S_6$ (CIPS) with the Cu atom positioned in the upper part of the layer, corresponding to upward polarization. Perspective view of two $[SCu_{1/3}In_{1/3}(P_2)_{1/3}S]$ layers. The c-lattice parameter is 13.09 Å. (b) Schematic of the sulfur octahedral cage showing the different types of copper sites: Cu atom can occupy the quasi-trigonal Cu^1 site (an off-centered site), the octahedral Cu^2 site (near the octahedron center), or the tetrahedral Cu^3 site (penetrating into the van der Waals (vdW) gap between layers). Each site has upward and downward symmetry-related positions. (c) The $P-E$ hysteresis loops of a 200 nm-thick CIPS parallel-plate capacitor measured at 1 kHz, confirming remanent polarization of 3.7 $\mu C\ cm^{-2}$. (d) PFM phase image of a 4 nm-thick CIPS flake with written box-in-box patterns by reverse DC bias. Scale bar, 1 μm. (e) Corresponding PFM amplitude (black) and phase (blue) hysteresis loops during the switching process, demonstrating switchable ferroelectric behavior. (f) Cross-sectional energy dispersive X-ray spectroscopy (EDS) mapping of Cu^+ distribution in a CIPS capacitor after prolonged DC bias stress, providing direct nanoscale evidence of Cu ion migration, indicated by a Cu-rich area. (g) PFM phase mapping by writing box pattern in CCPS nanoflakes with the thickness of 12 nm. (h) Off-field PFM phase and amplitude hysteresis loops measured in a 2.6 nm-thick CCPS nanoflake, confirming switchable ferroelectric behavior. (i) Schematic illustration of the interlayer antiferromagnetic order in CCPS, where only the Cr atomic layers are shown in lower panel. (j) Temperature-dependent $I-V$ characteristics of a CCPS device measured from room temperature (RT) to 250 °C. (a) Reproduced with permission.[151] Copyright 2020, Nature Publishing Group. (b) Reproduced with permission.[150] Copyright 2021, American Chemical Society. (c) Reproduced with permission.[129] Copyright 2021, Nature Publishing Group. (d and e) Reproduced with permission.[75] Copyright 2016, Nature Publishing Group. (f) Reproduced with permission.[153] Copyright 2020, Royal Society of Chemistry. (g and h) Reproduced with permission.[83] Copyright 2023, Nature Publishing Group. (i) Reproduced with permission.[86] Copyright 2024, Nature Publishing Group. (j) Reproduced with permission.[84] Copyright 2023, Nature Publishing Group.

off-centered quasi-trigonal Cu^2, and nearly tetrahedral Cu^3 within the vdW gap (Fig. 2b).[43,149–151] At low voltage, the Cu ions oscillate vertically within the octahedron (up and down positions), resulting in the upward and downward ferroelectric polarization (Fig. 2b). The local energy minimum occurs at a Cu ion displacement of 1.53 Å, with a calculated spontaneous polarization $P = \pm3.7\ \mu C\ cm^{-2}$ (Fig. 2c). When voltage or temperature exceeds a specific threshold, Cu ions may migrate to the vdW gap and form interlayer bonds with S atoms from neighboring layers (displacement of 2.25 Å, which corresponds

to $P = \pm11.26\ \mu C\ cm^{-2}$).[152] The velocity of Cu^+ ion along the polar is calculated to be $6.4 \times 10^{-7}\ s\ m^{-1}$, derived from the current evolution.[43]

CIPS is referred to as "ferroionic" due to the coexistence of dipole order (ferroelectricity) and ionic disorder (ionic conduction).[28] Within the framework of Cu activities in CIPS, four primary conductive mechanisms are identified in the Au/CIPS/Gr ferroelectric semimetal junction (FSMJ): frozen-in polarization state, ferroelectric polarization state (where Cu ions exclusively hop between Cu^{1u} and Cu^{1d} without escaping from

the sulfur framework), Cu ions hopping state (where Cu ion enter the vdW gaps and perform local hopping), and conductive filament state (where Cu ions migrate throughout the entire layer).[152] Furthermore, Cu ions can migrate in the in-plane direction with active energy of 0.23 eV (ref. 154) or 0.61 eV (ref. 150) when $T > T_c$, which are lower than the migration barriers in the out-of-plane direction of 0.85 eV (ref. 149) or 0.92 eV.[150] The migration pattern of Cu^+ ions is determined by activation energy. Some studies suggests that when a vertical voltage is supplied, Cu^+ ions initially follow an in-plane predominantly migration path before eventually migrating out-of-plane.[149] The coupling mechanisms between dipoles and Cu^+ ions have not been fully understood yet because the coupling occurs in nanoscale regions, which makes it challenging to clearly study the phenomena inside. Thanks to the rapid progress in *in situ* high resolution transmission electron microscopy (STEM) and scanning electron microscopy (SEM) with energy dispersive X-ray spectroscopy (EDS), researchers can acquire comprehensive information. In 2020, as reported by Zhou *et al.* in their EDS data, copper cations were observed to be mobile over the vdW layer and to accumulate near the cathode surface.[153] The sample utilized in their experiments is a metal/CIPS/metal capacitor, as shown in Fig. 2f. Since the discovery of ferroelectricity in 4 nm CIPS in 2016 (Fig. 2d and e),[75] various architectures of CIPS-based volatile and non-volatile memory devices have been proposed, demonstrating high performance and versatile functionality.

2.2.2 CuCrP$_2$S$_6$-based systems.

Diffusion kinetics of Cu^+ ions also occurs in $CuCrP_2S_6$ (CCPS) at room temperature. Despite the limited research on ferroelectric CCPS compared to CIPS, CCPS possesses a significant advantage: it exhibits ultra-high thermal stability at 120 °C (Fig. 2j),[84] substantially exceeding Curie point of CIPS of 42 °C. $CuCrP_2S_6$ (CCPS) has a thickness-independent dielectric constant of 35 by scanning microwave impedance microscopy (sMIM).[87] CCPS is a multiferroic material that exhibits coexistence of ferroelectric and ferromagnetic orderings within a single-phase material. The ferromagnetic and ferroelectric of $CuCrP_2S_6$ stems from magnetic Cr^{3+} ions (Fig. 2i) and displacement Cu ions, respectively and its magnetoelectric coupling[86] stems from the spin–orbit coupling.[81] CCPS has been shown robust room-temperature ferroelectric switching down to 2.6 nm (4 atomic layers) (Fig. 2h)[83] and square pattern with a phase contrast of ~180° were written and tested using PFM tips (Fig. 2g). The *P–E* hysteresis measurement exhibits remanent polarization and saturation polarization values of about 14.97 and 16.05 μC cm^{-2}, respectively, higher than that of CIPS.[83] With ferroelectric polarization, CCPS can be employed as the gate dielectric to realize hysteresis-free NC-FETs.[87] Furthermore, its switchable ferroelectric polarization can utilized to modulate interface charge injection, enabling the high-performance memristors[84] and part of one-transistor-one-memristor (1T1M) cells.[88]

2.3 Polarization-carrier coupling mechanism

2D ferroelectric materials that operate *via* the polarization-carrier coupling mechanism can be classified into ferroelectric semiconductors and ferroelectric metals (*e.g.*, WTe$_2$). Among ferroelectric semiconductors, three subtypes can be distinguished: in-plane ferroelectric semiconductors (*e.g.*, group IV monochalcogenides, MX; M = Ge, Sn; X = S, Se), out-of-plane ferroelectric semiconductors (*e.g.*, d1T-MoTe$_2$, Bi$_2$O$_2$Se), and intercorrelated ferroelectrics (*e.g.*, III$_2$–VI$_3$ compounds such as α-In$_2$Se$_3$). These materials exhibit unique polarization–carrier interactions, enabling efficient charge modulation and tunable electronic properties for neuromorphic applications.

2.3.1 In$_2$Se$_3$-based systems.

Indium selenide (In$_2$Se$_3$), a III–VI semiconductor, comprises five layers of Se–In–Se–In–Se with vdW interactions (Fig. 3a).[92] Bulk In$_2$Se$_3$ has been shown to exist in five distinct layered crystalline phases (α, β, γ, δ, κ), which arise from varying vertical stacking orders of the layers. α-In$_2$Se$_3$ exhibits two stacking configurations: a rhombohedral (3R) structure and a hexagonal (2H) structure, both are ferroelectric semiconductors, with the *c*-lattice constant 19.23 Å.[155] In$_2$Se$_3$ exhibits thickness-dependent bandgap (from 1.3 eV in bulk to 2.8 eV in monolayer).[156] Recently, the α-phase In$_2$Se$_3$, possessing an appropriate bandgap of 1.3 eV,[92,133,157] demonstrates several novel physical properties, including the bulk photovoltaic effect (BPVE),[158] the interplay of semiconductor and ferroelectric characteristics,[159] and the flexoelectric effect.[160] Its narrow and direct bandgap is more appealing for applications in visible and near-infrared optoelectronics.

In 2017, the ferroelectric properties of α-In$_2$Se$_3$ were first predicted, suggesting that α-In$_2$Se$_3$ might exhibit both out-of-plane and in-plane ferroelectricity at room temperature, even at the monolayer scale, with a calculated electric dipole moment of 0.11 eÅ per unit cell.[90] The displacement of selenium atoms in the middle Se layer generates spontaneous electric polarization.[92] In the same year, Zhou *et al.* reported the first experimental finding that the 10 nm thick α-In$_2$Se$_3$ demonstrates out-of-plane (OOP) piezoelectricity and ferroelectricity at room temperature.[91] Thinner α-In$_2$Se$_3$ materials were under investigation. Researchers subsequently confirmed the intercorrelated out-of-plane (OOP) and in-plane (IP) polarization in α-In$_2$Se$_3$ utilizing the chemical vapor deposition (CVD) method at a thickness of 6 nm (ref. 92 and 93) and exhibited stable ferroelectricity down to a monolayer (1.2 nm)[94] thickness in exfoliated α-In$_2$Se$_3$ nanoflakes (Fig. 3b). After that, α-In$_2$Se$_3$, a category of 2D ferroelectric material, has attracted significant attention in various fields related to ferroelectric devices.[119,162–166]

α-In$_2$Se$_3$ maintains the interlocked IP and OOP dipoles at room temperature (Fig. 3c). Rightward IP polarization is coupled with the downward OOP polarization, while the leftward polarization is coupled with the upward polarization (Fig. 3a). Therefore, unlike conventional ferroelectrics, the in-plane electric field in α-In$_2$Se$_3$ induces out-of-plane polarization switching, and the resulting polarization exhibits enhanced retention time.[133] Furthermore, the layer-dependent odd-even effect is observed: a flake with an even number of layers typically exhibits zero polarization, as the opposing polarizations in adjacent layers cancel each other out (Fig. 3e). α-In$_2$Se$_3$ is easy of scalability for large-area growth. The
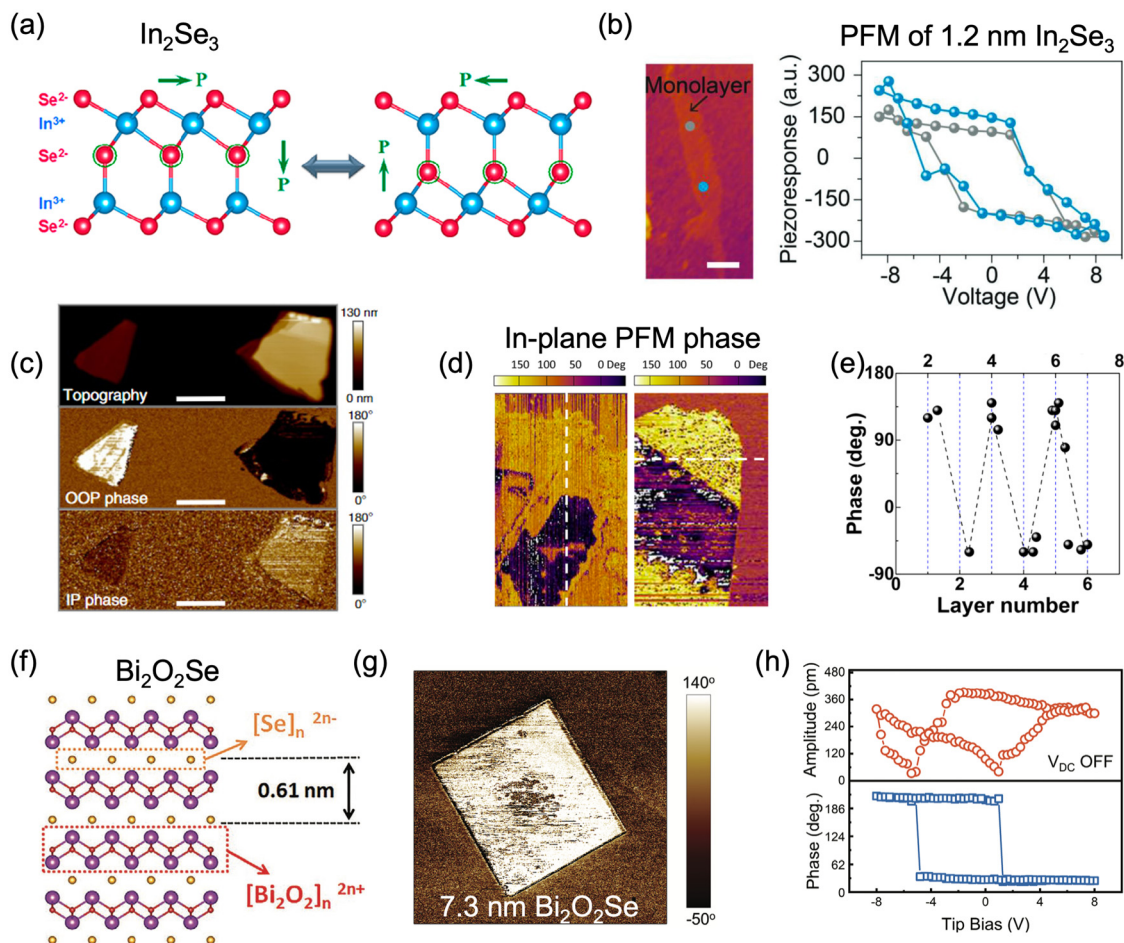
Fig. 3 Ferroelectric properties of ferroelectric semiconductor α-In$_2$Se$_3$ and Bi$_2$O$_2$Se. (a) Schematic model of interlocked in-plane (IP) and out-of-plane (OOP) ferroelectric polarization switching in α-In$_2$Se$_3$. (b) Ferroelectric hysteresis loop (right) measured in monolayer (1.2 nm) α-In$_2$Se$_3$ corresponding optical microscope image (left). (c) PFM phase mapping showing the coupling of OOP and IP polarization components. (d) Layer-dependent IP PFM phase images for α-In$_2$Se$_3$ films with thickness ranging from 2 to 6 nm. (e) Statistical analysis of the IP phase contrast as a function of layer number (1L to 6L), demonstrating the persistence and evolution of ferroelectric behavior with thickness. (f) Schematic illustration of the layered crystal structure of Bi$_2$O$_2$Se. (g) PFM phase image of a 7.3 nm-thick Bi$_2$O$_2$Se flake on Au film, deposited on a heavily p-doped silicon substrate. (h) Piezoelectric hysteresis loops conducted by applying DC voltage using DART-PFM, showing amplitude (top panel) and phase (bottom panel) response under DC field OFF, confirming ferroelectric behavior. (a, d and e) Reproduced with permission.[92] Copyright 2018, American Chemical Society. (b) Reproduced with permission.[94] Copyright 2018, Wiley-VCH. (c) Reproduced with permission.[161] Copyright 2022, Nature Publishing Group. (f) Reproduced with permission.[95] Copyright 2020, Wiley-VCH. (g and h) Reproduced with permission.[96] Copyright 2023, Wiley-VCH.

research presents inch-scale monolayer α-In$_2$Se$_3$ single crystals, representing a promising opportunity for the application of In$_2$Se$_3$ ferroelectric devices.[167] Vertically stacked α-In$_2$Se$_3$/WSe$_2$ heterostructures are directly synthesized by CVD and employed as photodetector, showcasing their potential uses in integrated optoelectronic devices.[168] It is noted that InSe is the same as In$_2$Se$_3$, is ferroelectric semiconductor, has an optical band gap of 1.25 eV.[169] A ballistic FET with 2D InSe as channel material exhibited performances that can surpass state-of-the-art silicon FETs.[170]

2.3.2 Bi$_2$O$_2$Se-based systems. Bismuth oxyselenide (Bi$_2$O$_2$Se, BOSe) is a ferroelectric semiconductor with out-of-plane ferroelectric property, in which both mobile free charges (attributable to its semiconducting nature) and polarized bound charges (owing to its intrinsic ferroelectricity) coexist

within the BOSe channel of FeS-FET.[96] At the atomic scale, BOSe exhibits several desirable electronic properties, including a tunable band gap (ranges from ~2.09 eV for monolayer[100] to ~0.8 eV for bulk state[96,97,99,100]). Furthermore, it possesses high carrier mobility (~410 cm^2 V^{-1} s^{-1}), high hall mobility (20 000 cm^2 V^{-1} s^{-1}), and low electron effective mass (0.14m_0), making it a promising material platform for high-performance ferroelectric semiconducting devices (Fig. 3f–h).[171]

2.3.3 SnTe and SnS-based systems. Both SnTe and SnS are semiconductors in their bulk form; however, they exhibit intrinsic in-plane (IP) ferroelectricity when thinned down to few-layer or monolayer thicknesses. In contrast to OOP ferroelectrics, reports on macroscopic devices exploiting IP ferroelectric switching remain scarce. While vertical device architectures are generally favored for high-density integration, lateral

devices also hold significant importance due to their potential for novel functionalities.

Bulk SnTe is a narrow-gap semiconductor (~0.2 eV) with a rock-salt structure and a lattice constant of 6.32 Å at room temperature. It is intrinsically heavily p-type doped, primarily due to the negative formation energy of Sn vacancies. Remarkably, IP polarization has been observed in SnTe down to the scale of just one unit cell,[101] attributed to the reduced screening effect of free carriers on dipole–dipole interaction. The carrier density depends on both the density of defects and the size of the band gap. In ultrathin SnTe films, the density of Sn vacancies is 2 to 3 orders of magnitude lower than that of bulk SnTe (Fig. 4b), and the bandgap significantly increases when the film thickness is less than 8 UC. These effects collectively lead to an enhancement in ferroelectric properties at the atomic scale. At the ferroelectric transition temperature T_c, SnTe undergoes a structural phase transition from a centrosymmetric cubic phase to a non-centrosymmetric rhombohedral phase. This transformation involves a relative displacement between Sn and Te sublattices (Fig. 4a), resulting in the spontaneous polarization. In the monolayer limit, this in-plane polarization is oriented along the x-axis.[101] Besides, a ferroelectric tunnel junction (FTJ) device based on in-plane polarization of SnTe demonstrates clear polarization-dependent tunneling behavior (Fig. 4c). When an in-plane write pulse is applied to generate an in-plane electric field, it induces two opposite in-plane polarization states, each producing different band bending. Subsequent readout *via* an OOP pulse to test electron tunneling, a hysteresis window is generated as the tunneling current is swept in opposite directions, achieving an on/off ratio of ~3000 (Fig. 4c).

Bulk Tin monosulfide (SnS) is a narrow-bandgap semiconductor (1.1 eV) with an interplanar distance of 3.1 Å, classified under the *Pnma* space group, and has feasibility for large-area CVD growth (Fig. 4d). Unlike other transition metal chalcogenides (TMCs), which are inherently n-type due to chalcogen vacancies, SnS is an intrinsically p-type semiconductor due to Tin vacancies. The reduced thickness of SnS enhances its ferroelectric properties. Thick SnS exhibits semiconductor characteristics, while thin SnS maintains room-temperature ferroelectric down to atomic scale (Fig. 4f) because of its lower carrier density and large band gap. The peak of thickness-dependent polarization current Fig. 4e indicates that the peak polarization current vanishes at greater thicknesses. The square hysteresis loop vanishes at greater thicknesses in the polarization–electric field (*P*–*E*) analysis (Fig. 4e). Some literature reports the remanent polarization to be about 17.5 μC cm^{-2} in more than one layer film,[105] while other suggest it to be slightly higher in monolayer SnS. The one reason is that the higher concentration of charge carriers in thick SnS obstructs the ferroelectric response due to the screening effect.[105] The other reason is that a thin structure breaks the lattice sym-
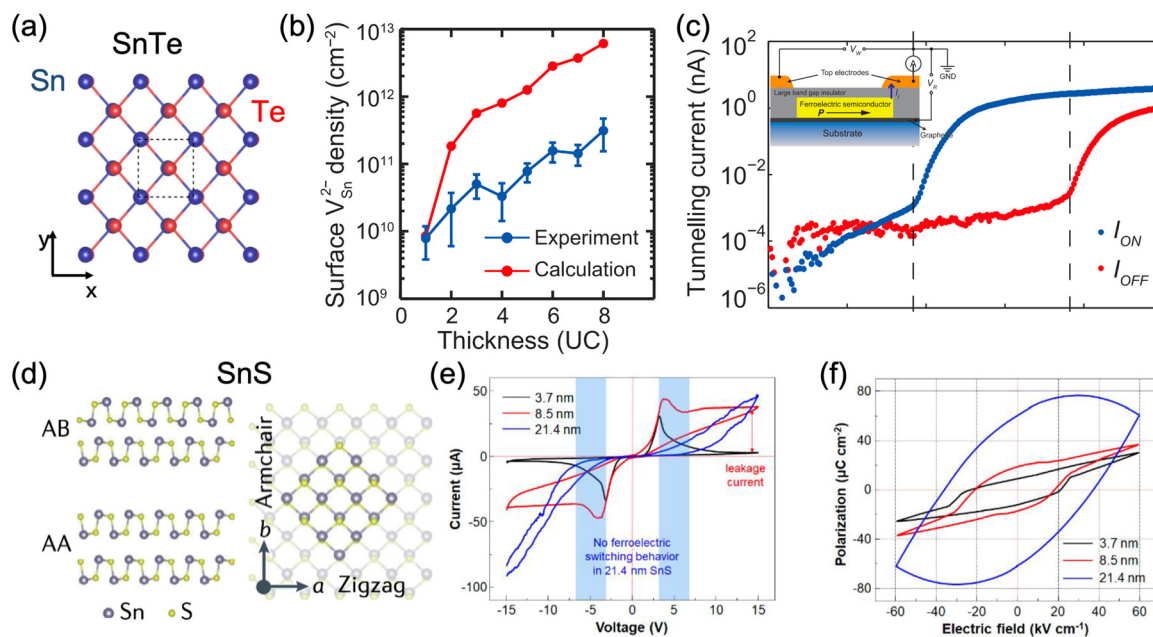
Fig. 4 In-plane ferroelectric properties of SnTe and SnS. (a) Schematic illustration of top view of the crystal structure of the SnTe monolayer. (b) Thickness-dependence of Sn vacancy density. (c) The tunnelling current exhibits a hysteresis loop, and a large on/off ratio is achieved. Inset: schematic of lateral device based on SnTe with in-plane polarization. (d) Cross-sectional crystal structures of SnS along the armchair direction with two different stacking configurations: non-centrosymmetric AA stacking and centrosymmetric AB stacking. (e) I-V curves of SnS thin film with varying thickness. Thicker SnS film exhibit the higher current levels and a slight shift in coercive field toward higher values. (f) *P*–*E* hysteresis loops of SnS thin film with varying thickness. (a) Reproduced with permission.[172] Copyright 2024, Springer Nature. (b and c) Reproduced with permission.[101] Copyright 2016, AAAS. (d) Reproduced with permission.[104] Copyright 2020, Nature Publishing Group. (e and f) Reproduced with permission.[105] Copyright 2020, American Chemical Society.

metry. Ferroelectricity arises from the breaking of inversion symmetry.

2.3.4 d1T-MoTe$_2$-based systems. Molybdenum ditelluride (MoTe$_2$) exhibits a direct bandgap of 1.2 eV in the monolayer form and an indirect bandgap of 1.1 eV in the bulk phase.[111] Most research on MoTe$_2$ focuses on the use of semiconductor channel layer in electronic devices.[37,148,173,174] In 2019, Yuan *et al.* reported the experimental observation of room-temperature OOP ferroelectricity in distorted 1T (d1T) MoTe$_2$ down to the monolayer limit, attributed to spontaneous symmetry breaking caused by the relative atomic displacements of Mo and Te atoms.[110] Additionally, Jindal *et al.* demonstrated that bilayer T$_d$-MoTe$_2$ exhibits ferroelectrics switching and superconductivity simultaneously.[175]

2.3.5 WTe$_2$-based systems. Ferroelectricity is usually observed in insulating or semiconducting materials rather than metallic ones, as itinerant electrons in metals screen out the electrostatic forces generated by long-range dipolar order and can also exclude external electric fields. In principle, intrinsic polarization in metals should only occur due to incomplete screening by mobile conduction charges.[107,109] Tungsten ditelluride (WTe$_2$) crystallized in an orthorhombic structure (T$_d$ phase), characterized by W atoms that are octahedrally coordinated by Te atoms, with successive layers rotated by 180° (Fig. 5a). WTe$_2$ is a topological semimetal that exhibits "metallic ferroelectricity" in bulk crystalline WTe$_2$ and in bilayer and trilayer configurations, while it becomes either a topological insulator or superconductor in the monolayer limit (Fig. 5b).[107,109] The coexistence of native metallicity and ferroelectricity in WTe$_2$ is attributed to the confinement of electron movement within the in-plane region, while the out-of-plane polarization results from interlayer sliding.[108,176]

2.4 Polarization-polarization coupling mechanism

The polarization–polarization coupling mechanism can be classified into two types. The first type occurs within a single material, where in-plane (IP) and out-of-plane (OOP) polarizations are interdependent—modulation in one direction can induce corresponding changes in the other. Representative materials exhibiting this behavior include CIPS and α-In$_2$Se$_3$. The second type involves coupling between two different ferroelectric materials, wherein the polarization dipoles of each material interact with one another. For example, inter-material coupling can arise from interactions between positive Cu$^+$ ions in CIPS and negative Se^{2-} ions in α-In$_2$Se$_3$.

2.5 Polarization-light coupling mechanism

Polarization reversal in ferroelectric materials is typically achieved through the application of an external electric field. However, recent studies have demonstrated that other external
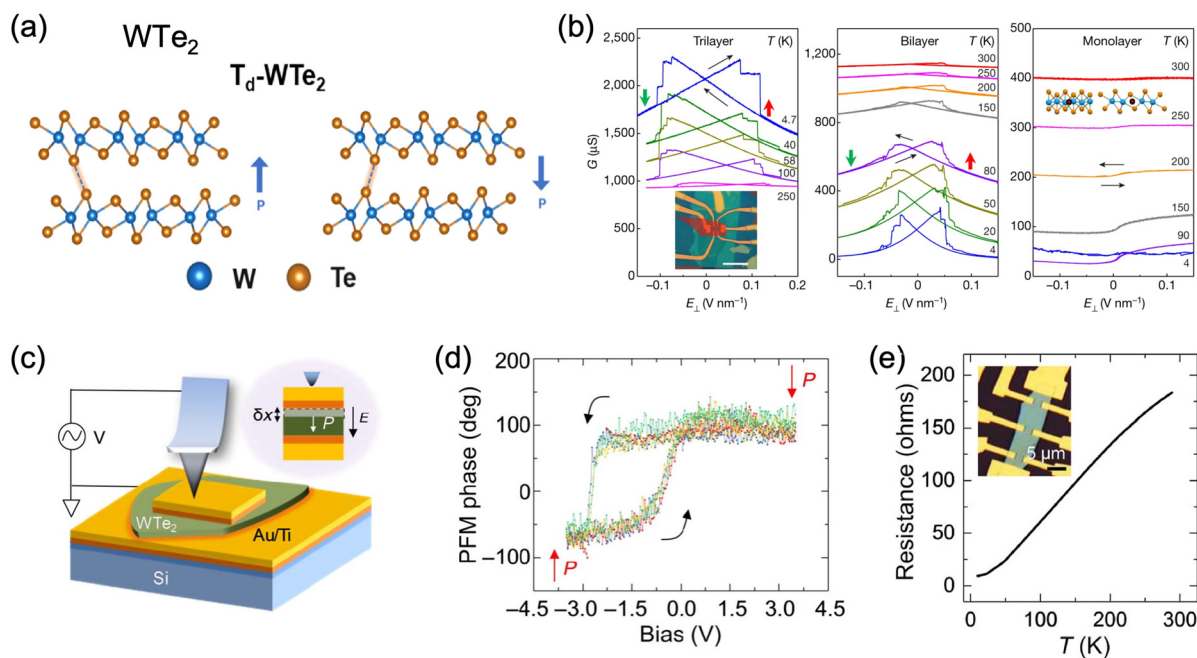
Fig. 5 Metallic ferroelectricity in WTe$_2$. (a) Side view of the crystal structure of multilayered T$_d$-WTe$_2$ illustrating up and down OOP ferroelectric polarization (indicated by blue arrows). (b) Electrical conductance G of undoped WTe$_2$ trilayer (left), bilayer (middle) and monolayer (right) devices as a function of sweeping electric field. The plots show bistable conductance states corresponding to upward (red arrows) and downward (green arrows), measured across a temperature from 4 K to 300 K. The undoped trilayer exhibits metallic temperature dependence, whereas the bilayer displays insulating behavior. (c) Schematic of a metal gated WTe$_2$ thin film device. (d) Piezoresponse phase hysteresis loops through the top metal electrode gate on the WTe$_2$ flake. (e) Temperature-dependent resistance of a 50 nm-thick WTe$_2$ sample measured from room temperature down to 10 K. (a) Reproduced with permission.[176] Copyright 2025, American Chemical Society. (b) Reproduced with permission.[107] Copyright 2018, Nature Publishing Group. (c−e) Reproduced with permission.[109] Copyright 2019, AAAS.

stimuli—such as mechanical stress, changes in the chemical environment, and light—can also induce polarization switching in certain ferroelectrics.[177–180] Among these, light is particularly attractive due to its non-contact and non-invasive nature, offering the potential for remote control of ferroelectric polarization.[181] This capability opens new opportunities for the development of photo-controlled ferroelectric devices, and significant progress has already been made toward realizing optical polarization switching.[163,177,182]

The coupling mechanisms between light and ferroelectric polarization can be broadly categorized into three types. First, optical absorption can induce structural modifications in the crystal lattice of ferroelectric material through combined photogalvanic, piezoelectric, or electrostrictive effects, thereby altering the polarization state.[132,137,158] Second, when a semiconductor is integrated into a ferroelectric device, photo-excitation in the semiconductor can redistribute screening charges, modulate the depolarization field, and potentially trigger polarization reversal.[162,183,184] Third, light absorption at material interfaces can lead to charge trapping, which, in turn, affects the internal electric field distribution and alters the ferroelectric properties of the device.[185,186] Collectively, these effects underscore the rich and dynamic interplay between light and ferroelectricity, highlighting the potential of polarization–light coupling for future multifunctional optoelectronic and neuromorphic device applications.[187–189]

3. Neuromorphic applications based on diverse coupling mechanism

Benefitting from the diverse coupling mechanisms discussed above, recent years have witnessed the rapid development of artificial devices based on 2D ferroelectric materials. These devices, particularly in the form of non-volatile and volatile memory elements, are considered as fundamental building blocks for neuromorphic computing systems. Fig. 6 illustrates some device structures that incorporate 2D ferroelectric as the functional layer to emulate the behavior of biological synapses. Structurally, these devices can be broadly classified into two-terminal and three-terminal configurations. The two-terminal category includes ferroelectric tunnel junction (FTJ) and ferroelectric diode (Fig. 6g–i), while the three-terminal category comprises ferroelectric field-effect transistor (FeFET) (Fig. 6b and c) and ferroelectric semiconductor field-effect transistor (FeS-FET) (Fig. 6d and e).

Two-terminal metal/ferroelectric/metal (M/F/M) structure (Fig. 6g–i), such as ferroelectric tunnel junction (FTJs) and ferroelectric diodes, are valued for their compact architecture and scalability. These devices typically exploit polarization-modulated Schottky-like barriers to achieve resistive switching. Among them, FTJs are particularly promising due to their ability to reversibly switch between high and low conductance states, characterized by the tunneling electroresistance (TER)
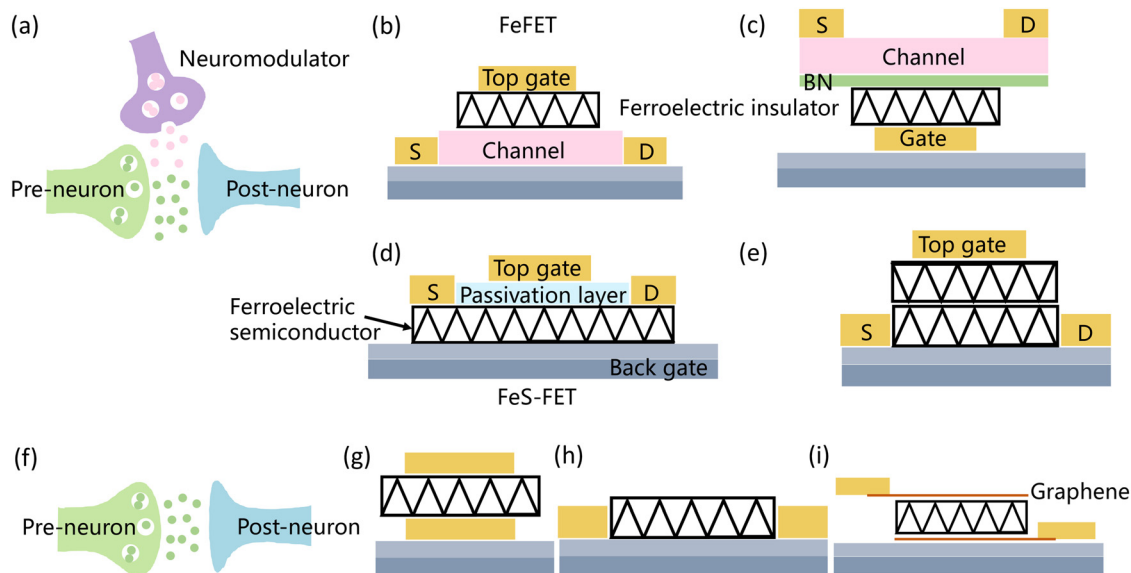
Fig. 6 Biological synapse architectures and its corresponding nanoelectronics artificial synaptic devices based on 2D ferroelectrics materials. (a) Schematic of a typical three-terminal biological synapse, illustrating the pre-neuron, post-neuron, and neuromodulator. (b) Schematic of a ferroelectric field-effect transistor (FeFET) utilizing a 2D ferroelectric material as the gate dielectric and a 2D semiconductor as the channel. The gate voltage acts as a neuromodulator. (c) FeFET configuration with the ferroelectric layer located beneath the channel. (d) Schematic of a ferroelectric semiconductor field-effect transistor (FeS-FET) employing a 2D ferroelectric material as the channel layer, with Al_2O_3 or BN used as the passivation layer. (e) Schematic of an all-ferroelectric FeFET structure utilizing 2D ferroelectric materials as the gate dielectric and channel layers. (f) Schematic of a two-terminal biological synapse. (g and h) Schematic diagrams of a metal/ferroelectric/metal vertical (g) and (h) lateral ferroelectric tunnel junction (FTJ) or ferroelectric diode fabricated on SiO_2/Si substrate, where the polarization direction modulates the Schottky barrier at the interface. (i) Illustration of polarization-induced doping in graphene device, in which the polarization charge can dope the graphene from nearly intrinsic to n-type or p-type, effectively tuning the barrier height.

ratio.[190] An FTJ typically consists of a nanometer-thick ferro-electric layer (<5 nm) sandwiched between two asymmetric electrodes. This configuration allows for low-voltages operation (several femtojoules per bit),[191] fast write/erase speeds (in nanosecond range), and nondestructive readout capabilities,[190] making FTJs strong candidates for next-generation, high-density memory and neuromorphic hardware applications.[192,193]

Among three-terminal devices, ferroelectric field-effect transistors (FeFETs) (Fig. 6b and c) have garnered significant attention due to their nondestructive readout capability, fast operation speed, compact footprint, and energy efficiency.[194] In these devices, 2D ferroelectric materials with wide bandgap are commonly employed as gate dielectrics. The Coulomb interaction between the ferroelectric polarization and the carriers in the semiconductor channel modulates the carrier concentration depending on the polarization direction, resulting in hysteretic behavior in the transfer characteristics.[195] The resulting channel conductance, which represents the synaptic weight, can be analogously tuned by voltage pulses, allowing for potentiation and depression of synaptic states. From a band structure perspective, polarization switching causes band bending, which is preserved due to the remanent polarization in the absence of gate voltage.[196] This intrinsic memory effect allows FeFETs to operate as both memory and synaptic devices, which is essential for in-memory computing architectures.[37,116,164,196-199]

Despite their potential, FeFETs face two major challenges: depolarization fields and leakage current.[194,200] The depolarization field arises because the dielectric constant of the semiconductor channel is often lower than that of the metal electrode, resulting in inadequate screening of ferroelectric polarization field.[201] Several strategies have been proposed to address this issue and improve the data retention. One solution is to employ high-k dielectric materials as the insulating layer to reduce the depolarization field.[202-204] Another approach is to eliminate the ferroelectric/insulator interface by using a metal-ferroelectric-semiconductor (MFS) structure with an oxide semiconductor channel.[53,165,205] Additionally, introducing a ferroelectric capacitor in series with the FET, either integrated with the FET or externally connected (MFMIS structure), can also help mitigate depolarization and degradation.[129,206] Selecting ferroelectric materials with better thermal stability, such as HfO_2,[59,207,208] has also shown to reduce the effects of depolarization, charge injection, and leakage current. Leakage current in FeFETs is often attributed to defects within the ferroelectric layer, poor crystal quality, or the formation of conductive filaments due to ion migration. This issue is particularly pronounced in two-dimensional ferroelectrics due to their ultrathin nature. Enhancing the quality of the ferroelectric film is therefore crucial for minimizing leakage current and ensuring reliable device performance.[177,194,196,209]

Moreover, the transfer characteristics (the drain current I_D versus the gate voltage V_G) of FeFET exhibit a clock or anti-clock hysteresis window during the forward and reverse V_G sweeps. The hysteresis is critical for memory and synapse operation, enabling multi-level conductance modulation. Clockwise hysteresis may arise from two mechanisms.[210,211] One is the tunneling of charge carriers' through the ferroelectric layer into the trapping layer, effectively screening the electric field and increasing the threshold voltage (V_{TH}). The other is charge trap phenomenon, resulting in charge carrier trapping and de-trapping due to the defect present at the interface between 2D channel layer and dielectric layer. In contrast, anti-clockwise hysteresis is primarily governed by the polarization switching direction, corresponding to the intrinsic counter-clockwise $P–E$ loop of the ferroelectric material.[196,212,213]

This section reviews several neuromorphic devices at the individual device level and highlights their significant contributions. Table 2 summarizes different coupling mechanisms in synaptic devices based on 2D ferroelectrics, along with their key merit, highlighting the distinctive properties and operational characteristics associated with each coupling mechanism.

3.1 Ferroelectric-dominated synaptic devices

Several two-terminal ferroelectric devices utilize the intrinsic ferroelectric properties of materials as their operational mechanism. Yu et al. constructed an artificial synapse based on a ferroelectric semimetal junction (FSMJ) using an Au/CIPS/Graphene structure, where gold (Au) and single-layer graphene (SLG) served as asymmetric electrodes. They identified the coupling between ferroelectricity and kinetics of Cu^+ ions, leading to a ferroelectric-dominated, dynamically tunable synaptic response that mimics the action potential biological afferents.[152] The device exhibits EPSC behavior due to gradual ferroelectric domain switching and displayed asymmetric current characteristics. This asymmetry was attributed to the internal built-in field in the ferroelectric layer—creating an asymmetric double-well potential with a preferred polarization direction—as well as to the work function difference in asymmetric electrode configurations, as seen in the Au/CIPS/Ti device.[147]

In the Au/CIPS/Ti device (Fig. 7a–f), ferroelectric polarization switching modulates the band alignment at the metal/CIPS interface. The device demonstrated a small set and reset voltage variation (σ/μ) of 5.3% and 9.1% compared to filamentary RRAM, with a low power consumption of 31 pW (standby) and 224 nW (set transition). It successfully emulated key synaptic behaviors, including PPF/PPD and STDP. The measured time constants for PPF (τ_a) and PPD (τ_b) were 12.2 and 10.8 ms, respectively (Fig. 7e), while STDP time constant are 8.3 ms ($\Delta T > 0$) and 20 ms ($\Delta T < 0$) (Fig. 7f), comparable to those observed in biological synapse. These findings validate the potential of the CIPS diodes employed in neuromorphic computing systems.
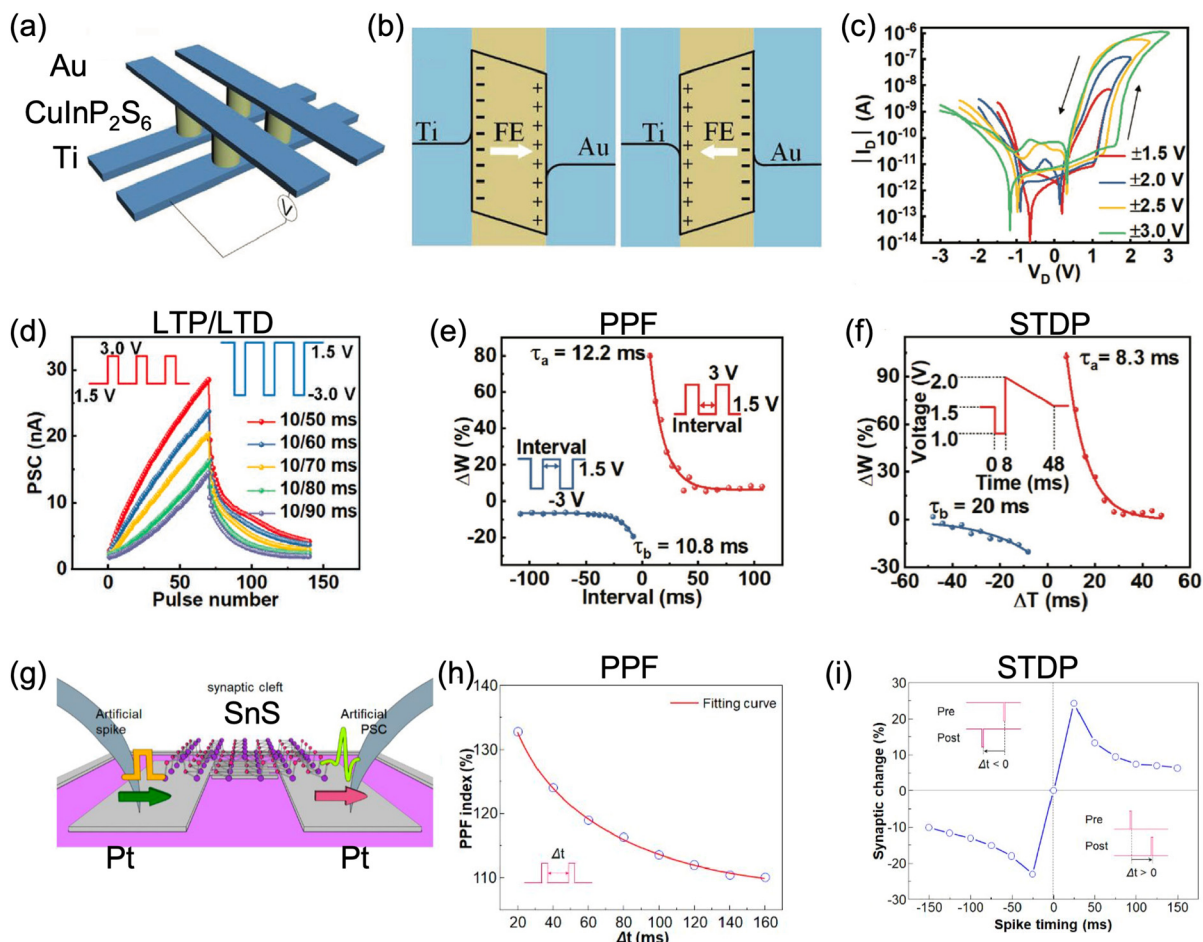
Although FTJ typically require asymmetric electrodes, ferroelectric materials can enhance the Schottky barrier at one interface while reducing it at the other, inherently inducing asymmetric transport behavior. Thus, symmetric electrodes

Table 2 Summary of different coupling mechanism types in synaptic device based on 2D FE, along with their key figures-of-merit (FOMs)

Coupling type	2D FE material	Structure	Memory window	On/off ratio	Endurance [cycles]	Retention [s]	Pulse width	LTP pulse number	Synaptic behavior	Other behavior	Ref.
FE-only	$CuInP_2S_6$	MoS_2/CIPS	2 V	10^5	10^3	10^3	1 ms			SS = 53.9 mV dec^{-1}	197
	$CuInP_2S_6$	CIPS/WS_2	3 V	10^7	—	—	—		STP, artificial neuromuscular;	Output current = 200 mA mm^{-1}	214
	$CuInP_2S_6$	CIPS/GaN	0.8 V	10^8	—	—	2 ms				215
	$CuInP_2S_6$	CIPS/WS_2/Al_2O_3	0.3 V	10^9	—	—	—			SS = 14 mV dec^{-1}. Low driven voltage of 0.3 V	216
	$CuInP_2S_6$	BN/MoS_2/CIPS/FLG					10 ms		EPSC, PPF, SADP		100
	$CuInP_2S_6$	CIPS/BN/InSe	4.6 V (clockwise)	10^4	10^3	10^4	40 ms				217
	$CuInP_2S_6$	CIPS/Gr/BN/MoS_2	3.8 V	10^7	10^4	4×10^3	100 ns				129
	$CuInP_2S_6$	CIPS/WSe_2	4.2 V	10^5	100	50			Memory ternary inverter.		218
	$CuInP_2S_6$	Gr/CIPS/Cr (FTJ)	—	10^6	10^4	10^4					219
	$CuInP_2S_6$	CIPS/GaN	0.5 V	10^8	—	—	1 ms	50	LTP, STP, artificial NMJ, artificial oculomotor dynamics	Normalized output current of 200 mA mm^{-1}	215
	$CuCrP_2S_6$	Au/CCPS/Au	—	10^3	10^3	10^3		30	LTP/LTD, SADP	Antiferroelectric.	84
	$CuCrP_2S_6$	CCPS/MoS_2	—	10^6	—	—				SS = 12 mV dec^{-1}	87
	α-In_2Se_3	In_2Se_3/GaN	2 V	10^{10}	10^3	—	1 ms	60	STP, RC	SS = 10 mV dec^{-1}	220
	α-In_2Se_3	Ti/In_2Se_3/Au	—	10^2	100	10^3			PSC, LTP/LTD, STDP. ANN.		221
	SnS	Pt/SnS/Pt	—	—	10^4	10^3	20 ms	100	EPSC, PPF, LTP/LTD, STDP, ANN		105
FE–ion coupling	$CuInP_2S_6$	Au/CIPS/Au	—	10^8		2×10^4	5 ms		LTP/LTD, SNDP, SRDP, PPF/PPD, potentiation following depression.		28
	$CuInP_2S_6$	Ni/CIPS/Ni	—	10^2	90	< 1	10 ms		LTP/LTD, PPF, reservoir Computing.		149
	$CuInP_2S_6$	Ag/CIPS/Au	—	10^3	500	10^4	30 ms		EPSC, PPF, LTP/LTD.		144
	$CuInP_2S_6$	Gr/CIPS/Gr	—	—	—	10^3					222
	$CuInP_2S_6$	Gr/CIPS/Cu	—	10^4	350	10^4	5 ms		EPSC, PPF, STP.		223
	$CuInP_2S_6$	Au/CIPS/SLG	—	10^2			5 ms			SS = 1.8 mV dec^{-1}	152
	$CuInP_2S_6$	Au-CIPS-Au	—	—	32	—	1 s	8000	PPF, STDP, Pavlov's dog, ADSP	Low power: 45 pJ per pulse	43
	$CuCrP_2S_6$	Au-CCPS-Au	—	—					LTP/LTD, CNN		224
	α-In_2Se_3	Ti/In_2Se_3/Au	—	10^3	100	10^4	20 ns		—		221

Table 2 *(Contd.)*

| Coupling type	2D FE material	Structure	Memory window	On/off ratio	Endurance [cycles]	Retention [s]	Pulse width	LTP pulse number	Synaptic behavior	Other behavior	Ref.
FE-carrier coupling	α-In$_2$Se$_3$	In$_2$Se$_3$/SiO$_2$ (3 nm)	16 V	10^8	—	—	—	100	PPF, LTP/LTD, CNN.	On-state power consumption = 10^{-5} W	225
	α-In$_2$Se$_3$	In$_2$Se$_3$/Al$_2$O$_3$/Si	12.4 V	10^6	10^3	10^4	10 ms	100	LTP/LTD, ANN	High linearity and symmetry.	226
	α-In$_2$Se$_3$	Al$_2$O$_3$/In$_2$Se$_3$/SiO$_2$	35 V	10^4	—	—	20 ms		STP (EPSC/IPSC. PPF.) LTP (STDP, SRDP.) STP-LTP transition.	Power consumption = 1 pJ.	34
	α-In$_2$Se$_3$	BN/In$_2$Se$_3$/BN/Al$_2$O$_3$	6 V	10^3	500	500	40 ns	30	PSC, SRDP, LTP/LTD. Iris recognition and classification.	Write speed = 40 ns. Energy consumption = 234/40 fJ.	155
	α-In$_2$Se$_3$	In$_2$Se$_3$/Ta$_2$O$_5$/Si	10 V	10^5	100	10^3	40 ms	100	PSC, PPF, ANN.	Nonlinearity = 0.12. Energy consumption = 10 pJ.	227
	α-In$_2$Se$_3$	Al$_2$O$_3$/In$_2$Se$_3$/Al$_2$O$_3$	13.5 V	10^5	250	150	100 µs	100	PSC, LTP/LTD, STDP. ANN.		228
	α-In$_2$Se$_3$	Al$_2$O$_3$/In$_2$Se$_3$/SiO$_2$	30 V	10^8	—	—	—	—			229
	α-In$_2$Se$_3$	Al$_2$O$_3$/In$_2$Se$_3$/HfO$_2$	2 V	10^8	—	—	—	—			229
	Bi$_2$O$_2$Se	Al$_2$O$_3$/Bi$_2$O$_2$Se/Mica	4 V	10^4	—	—	—	—			96
FE–FE coupling	CuInP$_2$S$_6$, α-In$_2$Se$_3$	CIPS/BN/In$_2$Se$_3$/CIPS	14.5 V	10^6	10^4	10^4	5 ms	64	EPSC/IPSC. LTP. CNN.		230
	SnS, CIPS	SnS/BN/CIPS	70 V	10^5	10^4	10^4	—	—		Four resistance states (two-bit storage)	231
	WTe$_2$, α-In$_2$Se$_3$	WTe$_2$/In$_2$Se$_3$/Au	—	10^5	—	—	—	—			176
	α-In$_2$Se$_3$ (OOP & IP)	MoS$_2$/BN/In$_2$Se$_3$/In$_2$Se$_3$	7.8 V	10^5	10^5	10^4	1 ms	100	LTP/LTD, CNN.		133
FE–optoelectronic coupling	CuInP$_2$S$_6$	Gr/CIPS/Au	—	—	—	—	50 ms	—			189
	CuInP$_2$S$_6$	SnS$_2$/hBN/CIPS	18.4 V	10^5	350	10^4	100 ms	—	PPF, STP, LTP/LTD. Reservoir computing. Retina-like adaptation. Pavlovian conditioning.		183
	CuInP$_2$S$_6$	ReS$_2$/hBN/CIPS	7 V	10^7	—	10^3	—	—	LTP; SRDP;		232
	α-In$_2$Se$_3$	Gr/In$_2$Se$_3$/Gr	—	10^2	60	60	—	60			166
	α-In$_2$Se$_3$	Au-In$_2$Se$_3$-Au	—	10^4	800	10^3	—	30		Optical PO + Electrical DE	233

Fig. 7 Two-terminal ferroelectric synaptic device operating solely *via* the intrinsic ferroelectric mechanism. (a) Schematic illustration of a vertical Au/CIPS/Ti device. (b) Energy band diagrams corresponding to two opposite polarization directions in the CIPS diode. (c) Measured I–V characteristics under varying voltage sweep ranges. (d) The PSC subject to trains of 70 positive (+3 V) and 70 negative (−3 V) pulse, pulse width is 10 ms, and pulse period is varied from 50 to 90 ms. (e) PPF and PPD results showing synaptic weight changes as a function of the inter-pulse interval. (f) STDP measurement of synaptic weight change as a function of the time interval between pre- and postsynaptic spikes. (g) Schematic of a planar Pt/SnS/Pt ferroelectric artificial synapse. (h) PPF index extracted from short-term plasticity enhancement with varying time intervals between two consecutive pre-synaptic spikes (3 V, 20 ms). (i) STDP behavior of the SnS-based ferroelectric synapse, demonstrating Hebbian learning rule with synaptic weight modulation dependent on relative timing of pre- and post-synaptic spikes. (a−f) Reproduced with permission.[147] Copyright 2020, Wiley-VCH. (g−i) Reproduced with permission.[105] Copyright 2020, American Chemical Society.

can also achieve FTJ-like functionality if a ferroelectric layer is centrally positioned. For instance, Kwon *et al.* presented a lateral Pt/SnS/Pt analogue synaptic device that employs the IP ferroelectricity of 6 nm-thick SnS (Fig. 7g). This device demonstrated key synaptic functionalities including PPF, LTP, and STDP (Fig. 7h and i), with robust endurance over 10^4 cycles, high linearity in potentiation/depression, multi-level conductance states, strong retention, and minimal variability across cycles and devices.[105] When evaluated using an artificial neural network (ANN), the system achieved a pattern recognition accuracy of 92.1% on the MNIST classification.

For three-terminal devices, CIPS is frequently used as a ferroelectric gate dielectric in FeFETs due to its relatively large bandgap among 2D ferroelectric materials. Numerous studies have demonstrated CIPS-based FeFETs with various 2D semiconductor, such as MoS_2[129,197,234–239] and WS_2.[214,216] Park

et al. fabricated a high-electron mobility transistor (HEMT)[215] utilizing CIPS as the gate dielectric and AlGaN/GaN as electron gas channel (Fig. 8a), emulating the biological neuromuscular junction (NMJ) and biological oculomotor dynamics. After enhancement, the device required fewer gate pulses to achieve higher EPSC, analogous to increased NMJ connectivity. A faster response time of 152 μs (Fig. 8b) was achieved compared to 297 μs without enhancement (Fig. 8c), demonstrating potential for neuromorphic vision and bioinspired robotics.

A similar structure incorporating α-In$_2$Se$_3$/GaN HEMT[220] (counterclockwise transfer curve is shown in Fig. 8d) was reported by Yang *et al.* The EPSC response to two pulses with a 100 μs interval showed clear temporal summation (Fig. 8e), enabling the implementation of reservoir computing (RC). When stimulated with a 3 × 5 binary image of the letter "A" (column-wise input: '01111', '10100', '01111'), the device gen-
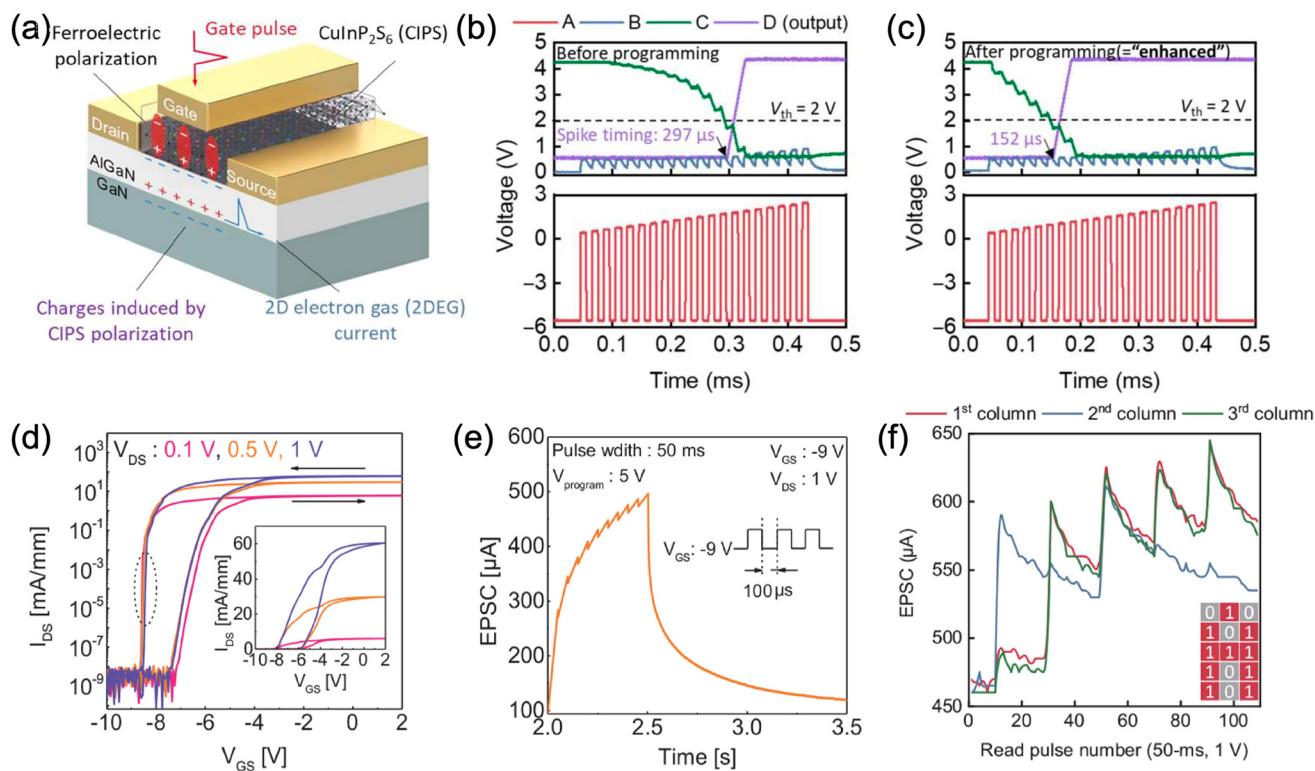
Fig. 8 FeFET-based artificial neural devices. (a) Schematic of a CIPS/GaN FeHEMT device. The polarization state in the CIPS can be modulated to emulate synaptic plasticity, while the resulting current in GaN channel serves as an artificial EPSC. (b) Output spike before programming and (c) after programming (enhanced). After the enhancement process, a nearly two times faster response (output spike) speed is observed. (d) I_{DS}–V_{GS} curve of GaN/In$_2$Se$_3$ MOS-HEMT. The inset shows the linear scale curve. (e) Cumulative EPSC response to sequential pulses with 100 μs interval. (f) Experimental EPSC response to the input pattern of the letter 'A', demonstrating the potential for neuromorphic classification tasks. (a–c) Reproduced with permission.[215] Copyright 2023, AAAS. (d–f) Reproduced with permission.[220] Copyright 2023, American Chemical Society.

erated distinguishable current patterns (Fig. 8f), which can be used as inputs for RC models for fast and efficient image classification.

3.2 Ferroelectric–ion migration coupled synaptic devices

Ion migration and defects are commonly recognized as key contributors to polarization switching instability and device degradation in many ferroelectric systems. For example, in hafnium zirconium oxide (HZO), the formation of oxygen vacancies is a primary cause of leakage current paths and unstable ferroelectric states.[60,240] Ion movement also underpins the operation of many resistive-switching devices,[241,242] in which the device typically exhibits a HRS due to insulating layers and switches to a LRS upon the formation of a conductive filament through the metal atoms migration.[19] Similarly, in 2D ferroelectric material-based devices, controlled ion migration plays a crucial role in mimicking the synaptic characteristics of biological systems. By precisely tuning ion dynamics, artificial synaptic and neural functionalities can be effectively emulated.

Two-terminal devices that rely on ion migration can be categorized into vertical and lateral structures. Similar to metal-filament-based memristors—commonly known as ReRAM—these devices generally adopt a metal/ferroelectric/metal con-

figuration.[243] The internal ferroelectric layer facilitates ionic conduction and resistance switching (RS) functionality. Notably, CIPS is a prototypical 2D ferroionic material, exhibiting both robust ferroelectricity and active Cu$^+$ ionic transport (Fig. 9a). In α-In$_2$Se$_3$, selenium vacancies (Fig. 9d) play a role analogous to oxygen vacancies in metal oxides, modulating the materials' valence state and resistance. Such devices are classified as valence change memories (VCM).[221] The coupling between ionic conductivity and ferroelectric switching can also give rise to novel phenomena, giving emerging applications in artificial synapses.

Experimental studies have demonstrated that CIPS-based devices driven by Cu$^+$ ion migration can emulate a wide range of neural functionalities.[28,144,147,149,152,222] For instance, in a lateral Au–CIPS–Au device (Fig. 9a),[43] several key synaptic functions have been successfully achieved, including STP, LTP, transition from STP to LTP, PPF, STDP, Pavlovian conditioning, and activity-dependent synaptic plasticity (ADSP). These functions arise from in-plane electric field-tunable ionic transport within CIPS. ADSP was demonstrated as follows: when a weak priming spike (4 V, 1 s) is applied, which alone does not induce any immediate variation in the device current, the subsequent application of a stronger voltage pulse (10 V, 1 s) leads to a PSC significantly higher than that induced by 10 V pulse
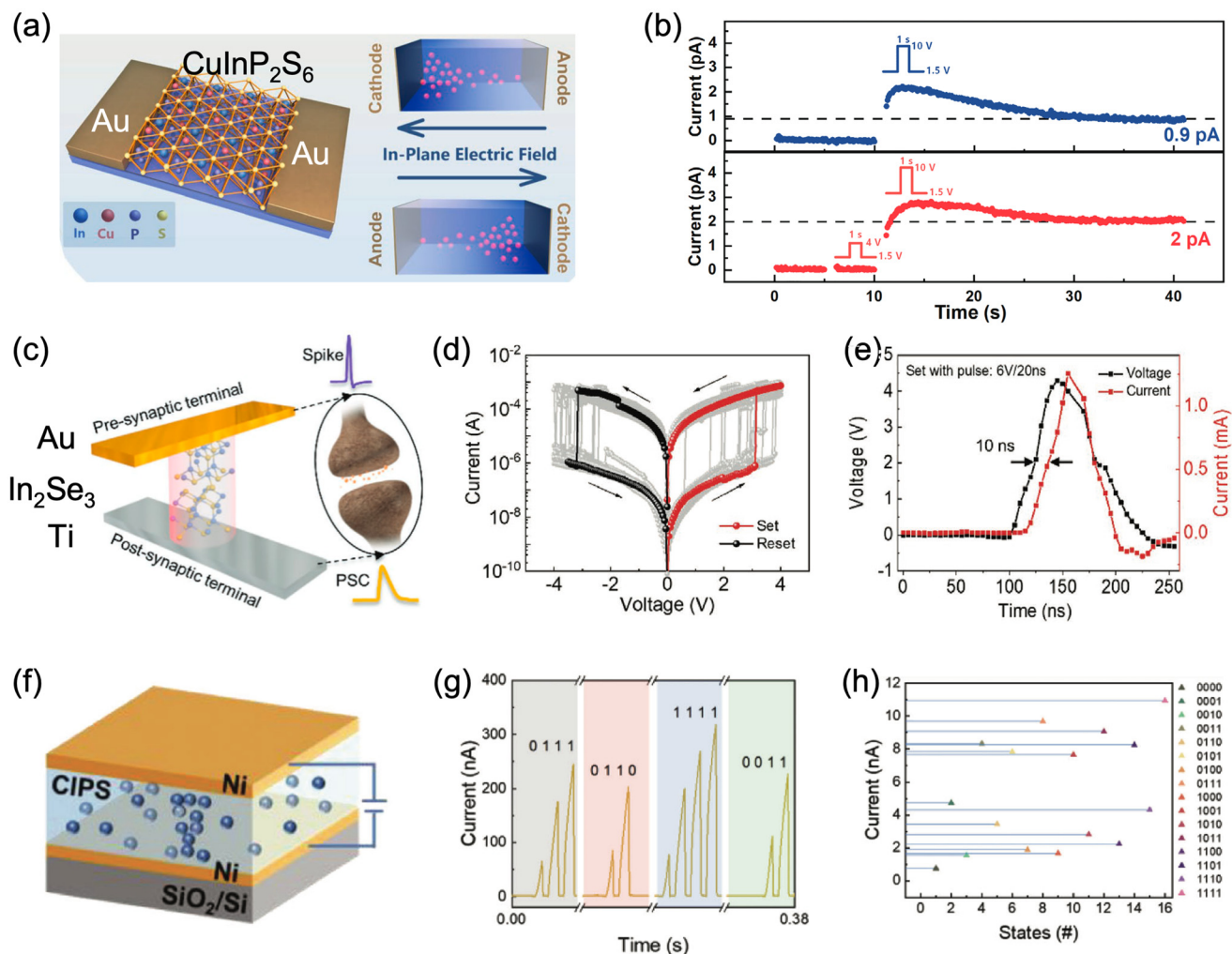
Fig. 9 Schematic illustrations and electrical characteristics of 2D ferroelectric device based on ion migration mechanism, demonstrating representative synaptic behaviors. (a) Schematic illustration of a lateral Au−CIPS−Au device, showing Cu^+ ion migration under an applied electric field. (b) EPSC responses under different stimulation protocols: the upper panel shows the EPSC induced by a single 10 V presynaptic spike; the lower panel shows enhanced EPSC when a 4 V priming spike precedes the 10 V presynaptic spike, demonstrating ADSP. (c) Schematic illustration of comparison between Se^{2+} vacancy migration in α-In_2Se_3 device and biological synapse. (d) 20 stable cycles of DC sweep of Au/In_2Se_3/Ti device after electroforming, attributed to filament-based switching. (e) High-speed switching characteristics during programming operations shows the device can be switched on within 10 ns. (f) Schematic of Cu^+ migration in vertical Ni/CIPS/Ni device. (g) Current response of a CIPS-based memory with a different pulse stream. (h) Current response to 16 different input states for reservoir computing. (a and b) Reproduced with permission.[43] Copyright 2022, Wiley-VCH. (c−e) Reproduced with permission.[221] Copyright 2021, Wiley-VCH. (f−h) Reproduced with permission.[149] Copyright 2024, Wiley-VCH.

alone. This prior-state-dependent plasticity arises from the partial migration of Cu^+ ions under initial weak electric field. Although the 4 V pulse does not significantly change the overall conductivity, it causes some Cu^+ ions to drift toward the cathode. These ions do not immediately return to their original positions, creating a metastable preconditioned state. As a result, the following high voltage pulse (10 V) drives more substantial ion migration, enhancing the EPSC amplitude (Fig. 9b). This mechanism can effectively mimic biological perception. For instance, a person transitioning from a cold to a hot environment may perceive the heat more intensely than someone already in a warm environment. Conversely, moving

from a hot to a cold environment may induce a sharper sensation of coldness than a transition between moderately cool environments. This analogy illustrates how ion migration-based synaptic devices can mimic perception in neuromorphic systems.

For vertical device architectures, Zhang *et al.* reported a crossbar-type Au/In_2Se_3/Ti device (Fig. 9c),[221] in which the memristive behavior is governed by the formation and rupture (set/reset processes) of conductive filaments originating from selenium vacancies. Following an initial electroforming step under a high voltage, the device exhibits abrupt and reversible switching behavior (Fig. 9d). Notably, the digital memory

mode can be set or reset by ultrafast electrical pulse with width of 20 ns, demonstrating high-speed digital memory performance (Fig. 9e). Furthermore, in a Ni–CIPS–Ni vertical device (Fig. 9f),[149] a forward voltage sweep from 0 to +2 V drives Cu^+ ions migration toward the cathode, resulting in a low resistance state (LRS). During the reverse sweep, Cu^+ ions accumulate at the interface near the cathode, restoring the device to a high resistance state (HRS). The electrical switching is attributed to the formation of an interfacial barrier and a build-in electric field, resembling the characteristics of a PN junction, enabled by mobile Cu^+ ions. The device exhibits short-term memory (STM) with a decay time of approximately 125.3 ms, indicating that its response is governed by both electrical excitation and natural relaxation dynamics. This transient behavior is utilized to simulate reservoir computing. Specifically, migration of Cu^+ ions in response to a binary "1" input generates a current spike, increasing conductance, while a "0" input allows the conductance to decay back to baseline (Fig. 9g). Using this mechanism, the system can encode and distinguish 16 different input sequences (Fig. 9h), highlighting its potential for use in neuromorphic computing architectures.

The strong intrinsic coupling between ferroelectric polarization and ion conduction in CIPS enables multi-modal neuromorphic functionalities. This dynamic control of various conductive switching mechanisms within a single device supports high-performance, energy-efficient neuromorphic computing systems. Xu *et al.* demonstrated a vertical Au/CIPS/Au device capable of tunable operation *via* both ionic migration and ferroelectric polarization (Fig. 10).[28] At high voltages, the device functions as a non-volatile memory driven by ionic effects, whereas at low voltages it operates as an artificial synapse controlled by ferroelectric polarization, exhibiting behaviors such as LTP, PPF/PPD, SNDP/SRDP (Fig. 10d–f). At intermediate voltages, cooperative interaction between ions and polarization produces "potentiation following depression" behaviors, related to pulse frequency. When operating as non-volatile memory, the device exhibits an ultra-high on/off ratio (10^8), long retention time (2×10^4 s), and multilevel resistance states enabled through current compliance engineering. At intermediate voltages, the interplay between ionic motion and ferroelectric switching mimics the biological Ca^{2+} ion channel and reproduces key synaptic behaviors of transition from PPF to PPD (Fig. 10c). High-frequency pulses (1 ms interval) induce ferroelectric polarization, mimicking Ca^{2+} influx and resulting in PPF, whereas low-frequency pulses (100 ms interval) promote Cu^+ ion migration, analogous to Ca^{2+} channel inactivation, resulting in PPD. These results underscore the potential of coupling of polarization and ion migration for modeling biological synaptic dynamics and enabling versatile neuromorphic functionalities.
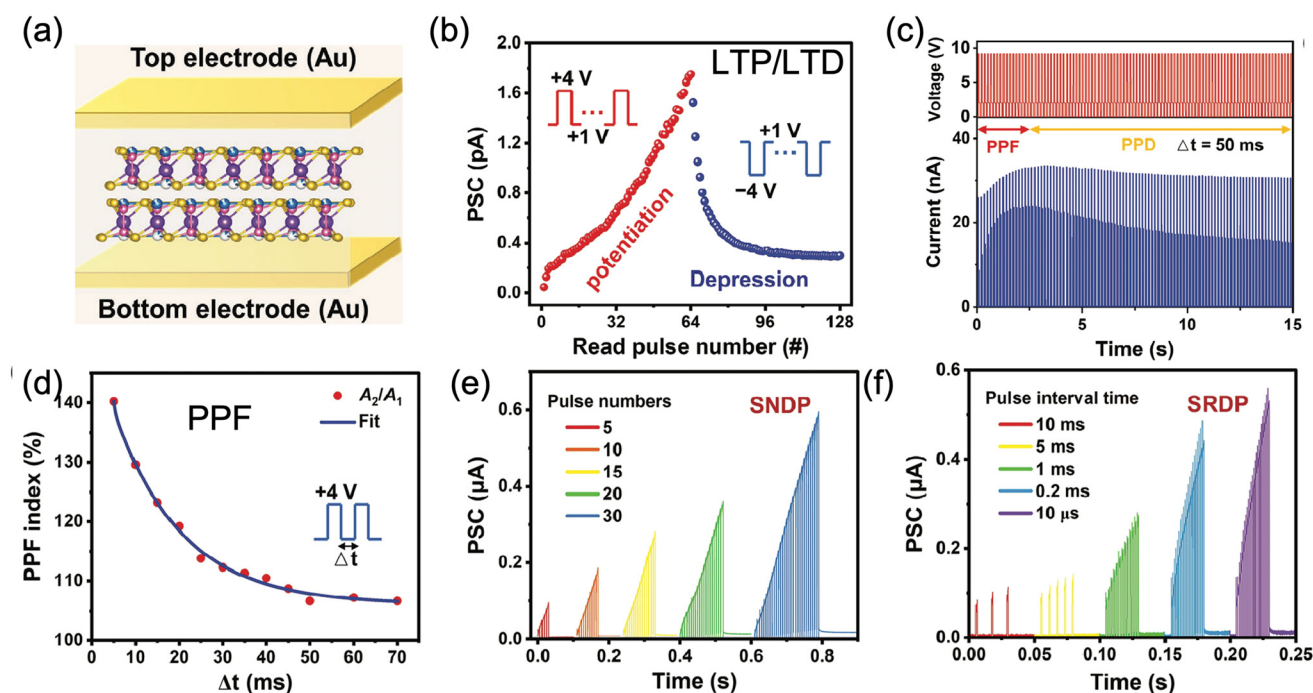
Fig. 10 Synaptic functions based on polarization and ion migration coupling mechanism on Au/CIPS/Au vertical device. (a) Structure schematic of CIPS-based vertical two terminal device. (b) Potentiation and depression characteristics under electrical stimulation. (c) Current response to consecutive electrical pulses with pulse interval of 50 ms and pulse width of 50 ms, demonstration the competition between ferroelectric polarization and Cu^+ ion accumulation/diffusion in the channel. An inflection from potentiation (PPF) to the depression (PPD) is observed as the number pulses increases. (d) PPF ratio as a function of time interval with corresponding fitting curve. (e) Spike number-dependent plasticity (SNDP) under varying pulse number. (f) Spike rate-dependent plasticity (SRDP) at different pulse frequency. (a–f) Reproduced with permission.[28] Copyright 2024, Wiley-VCH.

In addition, conductive filaments formation or the presence of selenium vacancies in α-In$_2$Se$_3$ and Bi$_2$O$_2$Se also represent ion migration-based mechanism.[98,127] When relying solely on intrinsic ferroelectric polarization, ferroelectric semiconductor junctions (FSJs) can be constructed using a 30 nm-thick α-In$_2$Se$_3$ layer embedded between single-layer graphene and few-layer graphene electrodes.[127] In this configuration, the ferroelectric polarization modulates the Schottky-like barrier at the graphene/In$_2$Se$_3$ interface. However, under high electric fields, significant defect formation may occur within the 2D ferroelectric, leading to the generation of conductive filaments. Unlike CIPS, where Cu$^+$ ions migration may not disrupt the ferroelectric polarization, α-In$_2$Se$_3$ device cannot fully recover their polarization functionality after electroforming, due to abundant selenium vacancies that facilitate metallic filament formation.[221]

3.3 Ferroelectric–semiconductor coupled synaptic devices

2D ferroelectric semiconductors, which simultaneously possess ferroelectric order (polarization-bound charges) and mobile charge carriers, can be classified into three categories: in-plane ferroelectric semiconductors (e.g., SnTe, SnS), out-of-plane ferroelectric semiconductors (e.g., Bi$_2$O$_2$Se, MoTe$_2$), and intercorrelated ferroelectric (e.g., α-In$_2$Se$_3$). In 2018, Si et al. reported the first ferroelectric-semiconductor-field effect transistor (FeS-FET) based on α-In$_2$Se$_3$ (Fig. 11d–f).[229] Since then, FeS-FET employing ferroelectric α-In$_2$Se$_3$ as the channel material and various gate dielectrics have been extensively studied.[34,155,225–228,244] These devices offer significant advantages over conventional FeFET, as the presence of mobile charges allows for screening of the depolarization field, mitigating charge trapping and leakage currents, which leads to enhanced retention time and improved endurance cycles.[155,227,229] For example, an In$_2$Se$_3$-based FeS-FET with HfO$_2$ gate dielectric exhibits a wide memory window, an exceptionally high on/off ratio (10^8), a maximum on-state current of 862 μA μm^{-1}, and operates under a low supply voltage,[229] making it highly attractive for artificial synapses applications.

The hysteresis direction in the transfer characteristics of FeS-FET depends on the effective oxide thickness (EOT) of dielectric materials (Fig. 11). High-EOT materials (e.g., 270 nm SiO$_2$) (Fig. 11a and d) typically exhibit clockwise hysteresis, whereas low-EOT materials (e.g., 10 nm Al$_2$O$_3$ or 15 nm HfO$_2$) (Fig. 11b and e) show counterclockwise hysteresis.[96,229] This behavior arises from the different extents of polarization switching within the ferroelectric semiconductor. In high-EOT devices, the electric field penetrating through the ferroelectric semiconductor cannot reach its top surface, resulting in partial polarization switching near the oxide/semiconductor interface. Consequently, the channel current is dominated by mobile charges at the bottom surface. When the polarization points downward, mobile charges accumulate at the bottom surface, leading to high channel current. This behavior corresponds to a clockwise hysteresis loop. In contrast, in low-EOT devices, the electric field is enough to induce full polarization switching in ferroelectric semiconductor. Here, the channel current is dominated by the charge at the top surface. When
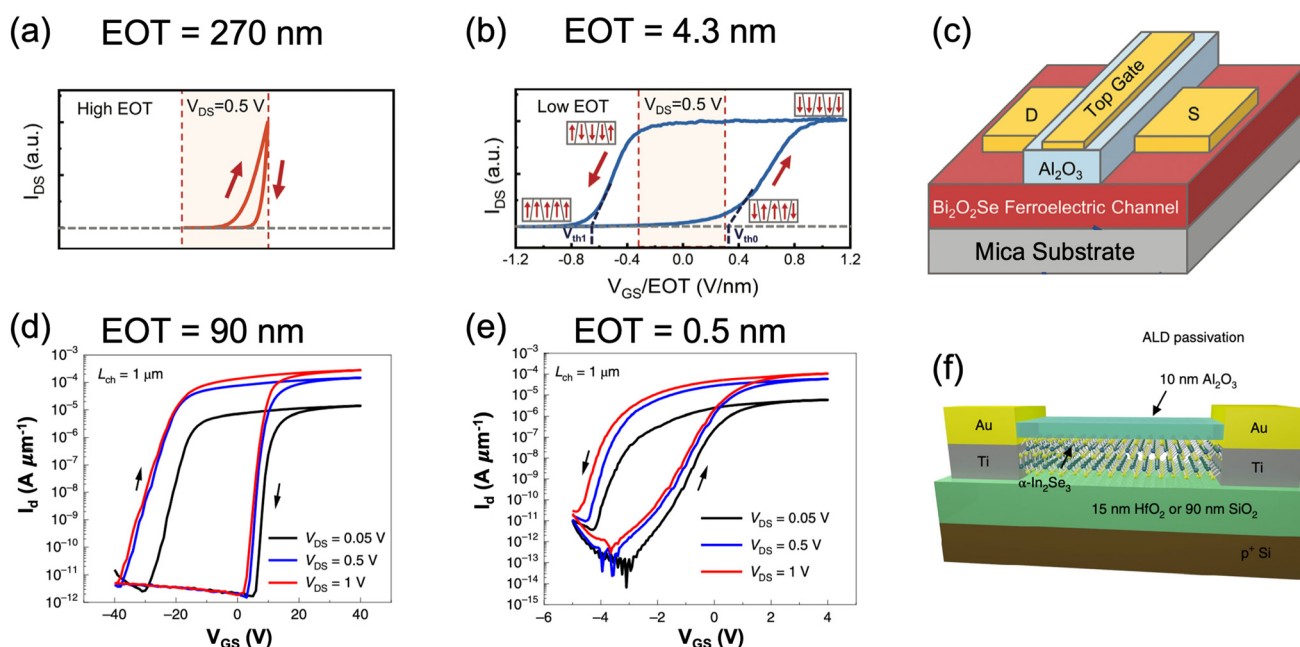
Fig. 11 Influence of hysteresis direction and equivalent oxide thickness (EOT) of dielectric materials on FeS-FET characteristics. (a and d) The clockwise I_d–V_g curves observed when using a large-EOT dielectric. (b and e) Anticlockwise I_d–V_g transfer curves observed with a small-EOT dielectric. (c) Schematic diagrams of Bi$_2$O$_2$Se-based FeS-FET corresponding to the electrical behaviors in (a) and (b). (f) Schematic diagrams of In$_2$Se$_3$-based FeS-FET corresponding to electric properties in (d) and (e), illustration the correlation between dielectric properties and hysteresis direction. (a–c) Reproduced with permission.[96] Copyright 2023, Wiley-VCH. (d–f) Reproduced with permission.[229] Copyright 2019, Nature Publishing Group.

the polarization points downward, mobile charges do not exist at the top surface, resulting in high channel resistance, reinforcing the observed counterclockwise hysteresis loop. Additionally, the bottom surface is much easier to be modulated by the gate voltage.

In FeS-FETs using 2D ferroelectric semiconductors, synaptic functionality can be achieved by applying electric pulses either to the drain terminal or the gate terminal, offering versatile modes of synaptic operation. Notably, these devices can operate without an additional semiconductor channel layer. When a negative pulse is applied to the drain terminal (Fig. 12a–c), it induces an abrupt drop in current followed by a rapid recovery, and PPF shows the enhancement of PSC under positive pulse (Fig. 12b). The corresponding $I_{ds}–V_{ds}$ characteristics display a butterfly-like hysteresis loop (Fig. 12a). In contrast, when pulse is applied to the back-gate terminal (Fig. 12d–f), a negative pulse consistently generates an excitatory PSC (Fig. 12e). To compare LTP (Fig. 12c and f) of synaptic learning behavior, Chen *et al.*[226] conducted a study between drain-terminal and gate-terminal pulsing. Pulses applied to the drain terminal achieved superior performance with near-ideal linearity (nonlinearity factors of 0.207 and 0.211) and excellent symmetry (asymmetry value of 0.004), along with the capability of supporting 100-level conductance states, demonstrating superior performance compared to gate terminal pulsing. The underlying mechanism of the drain terminal modulation is attributed to the coupling between in-plane polarization and channel conductivity, whereas gate-terminal modulation relies on the coupling between out-of-plane polarization and conductivity.

FeS-FET have been successfully integrated with various conventional dielectric materials, including h-BN, SiO_2,[34,225,244] Al_2O_3,[228] HfO_2, *etc*. Therefore, different dielectric choices may lead to different performance of FeS-FET. For example, Mohta *et al.* employed Ta_2O_5 as a high-k dielectric to reduce energy consumption and improve tunneling efficiency, using a bottom gate configuration.[227] This approach also enhanced the nonlinearity of synaptic weights updates and enabled the

Drain terminal modulation

Gate terminal modulation
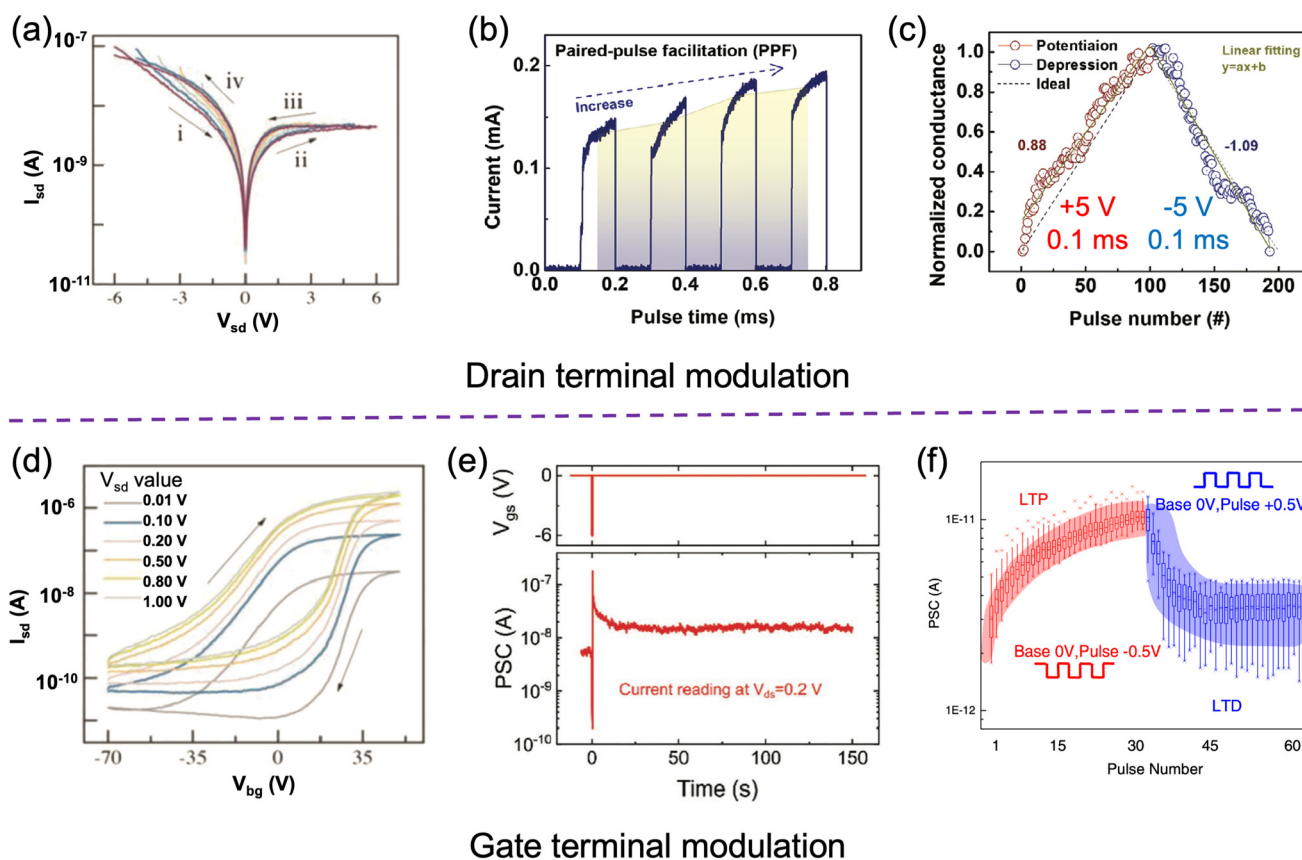
Fig. 12 Dual-pulse modulation schemes in FeS-FET based on an α-In_2Se_3 device for emulating synaptic behavior. Electrical characteristics under drain terminal modulation (a, b and c) and gate terminal modulation (d, e and f) are shown. (a) $I_{sd}–V_{sd}$ curves under increasing range of V_{sd} from 2.0 to 6.0 V, demonstrating typical drain-terminal modulation behavior. (d) $I_{sd}–V_{bg}$ curves at different V_{sd} values, exhibiting the characteristic anticlockwise hysteresis under back-gate modulation. (b) PPF measured under 5 V, 0.1 ms pulse applied to the drain, showing enhancement of PSC under positive pulse. (e) PSC response to a negative pulse at the gate terminal, indicating excitatory synaptic behavior. LTP and LTD characteristics under drain (c) and gate (f) terminal modulation. (a and d) Reproduced with permission.[34] Copyright 2021, Wiley-VCH. (b and c) Reproduced with permission.[225] Copyright 2025, Wiley-VCH. (e) Reproduced with permission.[228] Copyright 2020, Wiley-VCH. (f) Reproduced with permission.[155] Copyright 2021, Nature Publishing Group.

demonstration of linear weight modulation and spike time dependent plasticity (STDP) behavior as artificial synapses. Beyond the vertically stacked FeS-FET, planar memristor structures based on α-In$_2$Se$_3$ with an inserted 3nm SiO$_2$ layer has also been demonstrated. These devices exhibit an enhanced memory window (16 V), high on/off ratio (10^8), and improved linearity. On-chip training of single-layer perception (SLP) and convolutional neural network (CNN) has achieved classification accuracy up to 90%, highlighting their strong potential for neuromorphic computing systems.[225]

3.4 Ferroelectric–ferroelectric coupled synaptic devices

When two ferroelectric materials are integrated into a single device, the resulting FeFET exhibits enhanced polarization retention due to the coupling effect between the remanent polarization of both ferroelectric materials. This interfacial coupling significantly improves non-volatile storage capabilities.[164] For instance, a heterostructure composed of BiFeO$_3$ and α-In$_2$Se$_3$ exhibits an extended retention time exceeding 1000 s at 380 K,[164] highlighting its potential for high-performance memory applications with improved endurance and reliability. Based on this concept, in 2022, Lee *et al.*[230] reported an all-2D-ferroelectric FeFET composed of a layer of ferroelectric dielectric CIPS and a layer of ferroelectric semiconductor α-In$_2$Se$_3$ (Fig. 13a). Analysis based on Landau–Khalanikov (L–K) theory confirmed that this vertically stacked dual-ferroelectric configuration enhances both the ferroelectric properties and the memory hysteresis window. Owing to the presence of polarization-bound charges in both the gate dielectric and channel layer, interfacial dipole coupling occurs at the α-In$_2$Se$_3$/CIPS interface, where Cu$^+$ ions migrate upward and Se^{2-} ions move downward (Fig. 13b). This interfacial interaction stabilizes the polarization states, leading to prolonged retention with no observed degradation (Fig. 13d) and a significantly enlarged hysteresis window of 14.47 V (Fig. 13c), surpassing that of α-In$_2$Se$_3$ FeS-FET using conventional HfO$_2$ dielectrics. In addition to non-volatile memory capabilities, the device demonstrates essential synaptic functionalities, including EPSC/IPSC, PPF, and LTP/LTD. By applying 64 excitatory and 64 inhibitory pulses, the conductance was modulated (Fig. 13e). A convolutional neural network (CNN) implemented with this device achieved an image recognition accuracy of 84.2%, underscoring its applicability in brain-inspired computing.

Niu *et al.* developed a bidirectional polarization integrated FeFET[231] by combining IP ferroelectric semiconductor SnS and OOP ferroelectric dielectric CIPS (Fig. 13f), exhibiting excellent endurance (10^4 cycles) and retention (10^4 s). The device features four distinct resistance states—HRS, mid-HRS, LRS, and mid-LRS—arising from the combination of the two polarization states in each material. This multi-bit capability is realized without the need for intermediate state transitions, as the OOP and IP polarization states can be independently controlled using vertical and lateral electric fields, respectively (Fig. 13g). Specifically, the vertical gate voltage (V_G at terminal T2) modulates the channel carrier density through polariz-

ation-induced charge accumulation, while the lateral drain–source voltage (V_{DS} at terminal T1) modifies the band alignment between the channel and electrodes, thereby regulating charge injection and extraction (Fig. 13f).

In related architecture, a ferroelectric semiconductor junction (FSJ) utilizing ferroelectric metal WTe$_2$ as one of the electrodes in a WTe$_2$/In$_2$Se$_3$/Au[176] exhibits three distinct resistance states: on, off, and an intermediate state, within a wider applied voltage range from −3.5 V to 3.5 V (Fig. 13h). Unlike the dual polarization switching CIPS/In$_2$Se$_3$ FeSFET, *in situ* Kelvin probe force microscopy (KPFM) verified that the WTe$_2$ top layer retains its unchanged upward direction under external voltage (Fig. 13i). The observed multi-resistance behavior arises from the modulation of the Schottky barrier height due to α-In$_2$Se$_3$ polarization switching. Upward polarization in α-In$_2$Se$_3$ results in electrons accumulate at the WTe$_2$/In$_2$Se$_3$ interface, leading to downward band bending in WTe$_2$ and a low resistance on state. Conversely, when a downward external electric field is applied, the band of WTe$_2$ bend upward, the polarization in α-In$_2$Se$_3$ is completely reversed downward, increasing the Schottky barrier by 0.37 eV (calculated as 5.12 eV–4.75 eV) compared to the on state. This increase suppresses thermionic emission, thereby elevating the device resistance and switching it into the off state. Partial polarization reversal and pinning effects contribute to the stable intermediate state, making the device a promising candidate for mimicking analog synaptic behavior.

Additionally, polarization coupling is not limited to interactions between separate materials; it can also occur within a single material system. For example, laterally gated (LG) FeFET based on α-In$_2$Se$_3$[133] and CuInP$_2$S$_6$[42] demonstrate that coupling between IP and OOP polarization can also enhance retention time and expand memory window, offering an additional pathway to optimize ferroelectric memory performance.

3.5 Ferroelectric–optoelectronic coupled synaptic devices

Some 2D ferroelectric materials exhibit excellent optical properties and strong light–matter interactions, enabling light information to be stored and retrieved *via* ferroelectric domains or domain walls. This capability facilitates the development of optoelectronic memories and optoelectronic artificial synapses (Fig. 14a and b). Unlike conventional electronic memory or synapse that rely solely on electrical stimulation, optoelectronic artificial synapses utilizing both electrical and optical stimuli to modulate synaptic weights (light write and electric erase).[161,166,183,232,233] This dual-mode operation enables the device with both data storage and light-sensing capabilities. The integration of sensing, memory, and neuromorphic functionalities within a single device presents a promising platform for advanced neuromorphic vision systems. These hybrid systems emulate the biological retina's functionalities, laying the foundation for neuromorphic vision sensors and expanding the versatility of brain-like neural networks.[245]

2D ferroelectric materials with narrow bandgap and high carrier mobility are particularly suitable for next-generation
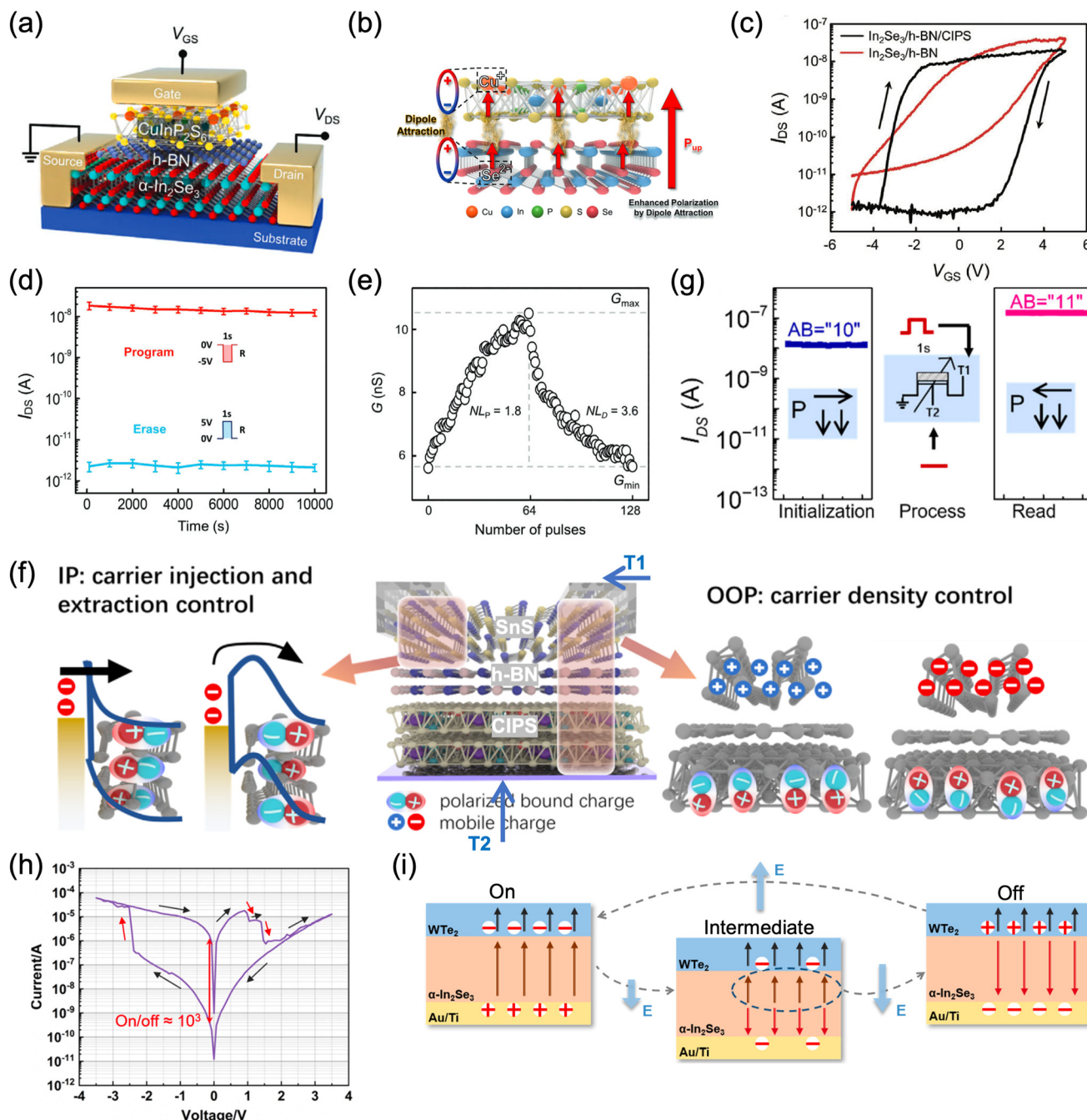
Fig. 13 Device based on ferroelectric-ferroelectric coupling mechanism. (a) Schematic of the all-ferroelectric device composed of 52 nm α-In$_2$Se$_3$, 6 nm BN, and 84 nm CIPS. (b) Schematic atomic model illustrating the upward polarization state in the In$_2$Se$_3$/CIPS heterostructure. (c) Transfer characteristics (I_D–V_G) showing a significantly larger hysteresis window in the CIPS/BN/In$_2$Se$_3$ device compared to the In$_2$Se$_3$/BN device, attributed to the polarization coupling between the two ferroelectrics. (d) Data retention characteristic measured over 10^4 s following programing/erasing pulse. (e) LTP/LTD behavior under 64/64 excitatory/inhibitory pulses ($\pm$0.5 V, 5 ms), demonstrating nonlinearity factors of 1.8/3.6. (f) Schematic of a bottom-gated dual-ferroelectric device with ferroelectric SnS as the channel material and CIPS as the ferroelectric gate dielectric. The schematic illustrates charge density and injection modulation *via* OOP/IP polarization under two programming condition (T1 and T2). (g) Demonstration of direct transition between multilevel resistance states, using the "10" state to the "11" state as an example. Left: initial state, middle: applied operation, right: final state. (h) Electrical transport characteristics of WTe$_2$/In$_2$Se$_3$/Au FSJ, showing a plateau of an intermediate resistance state. (i) Schematic illustration of the three different ferroelectric polarization states in the WTe$_2$/In$_2$Se$_3$/Au FSJ device, corresponding to three distinct resistance levels. (a–e) Reproduced with permission.[230] Copyright 2022, Wiley-VCH. (f and g) Reproduced with permission.[231] Copyright 2024, Wiley-VCH. (h and i) Reproduced with permission.[176] Copyright 2025, American Chemical Society.
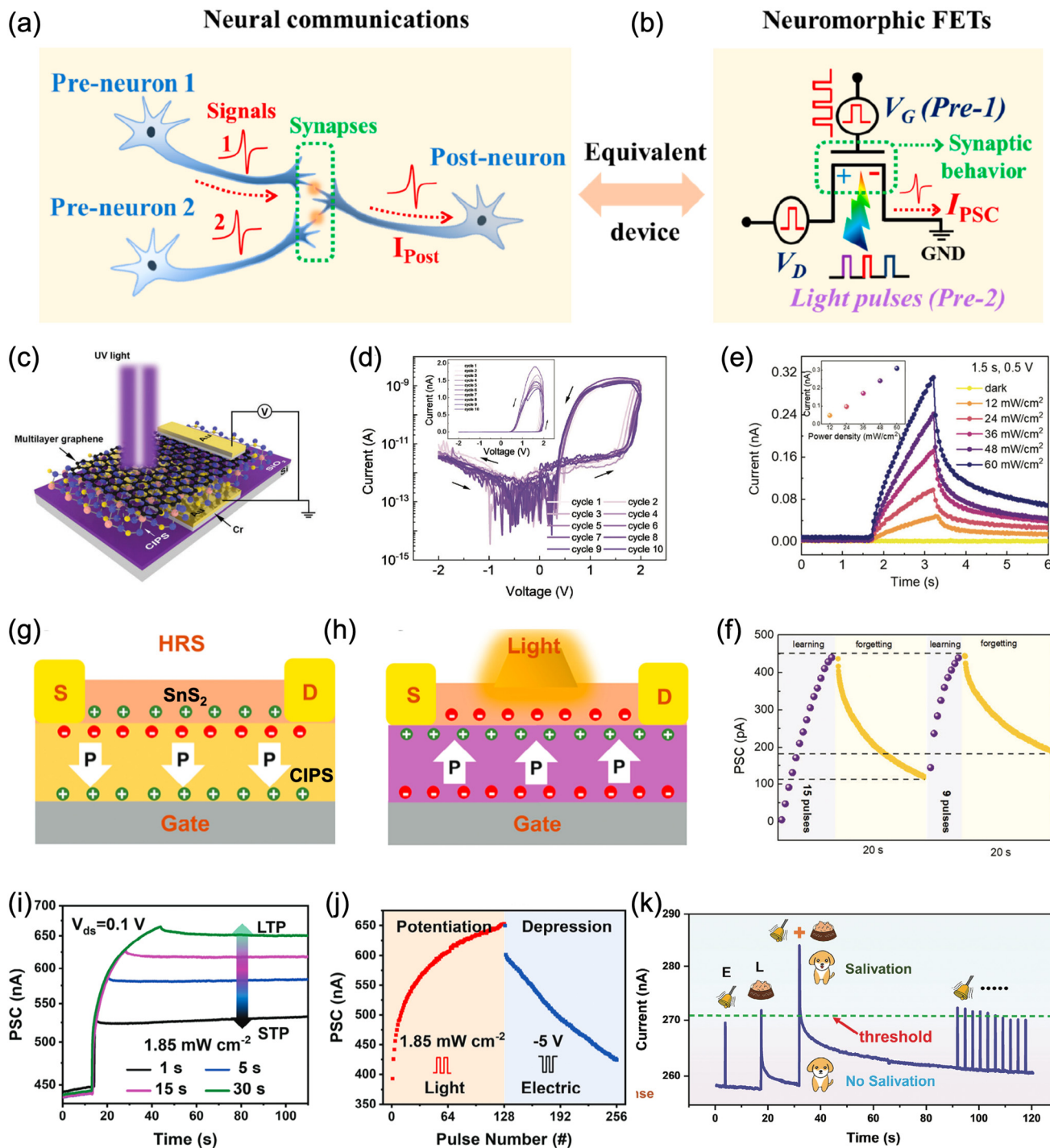
Fig. 14 Polarization-light coupling mechanism in 2D FE optoelectronic synapses. (a) Schematic illustration of a biological light-sensitive synapse (a) and its electronic counterpart (b). (c) Schematic diagram of the ML graphene/CIPS/Au electronic/optoelectronic device. (d) Ten consecutive I–V sweeps within ± 2 V. The inset shows the linear-scale I–V curves highlighting rectification. (e) Photocurrent responses under light pulses of various power densities; inset plots the peak photocurrent as a function of incident power. (f) Optical "learning-forgetting-relearning" process under sequential light stimulation. (g) Architecture of a three-terminal SnS_2/h-BN/CIPS Fe-FET optoelectronic device and schematic illustration of polariz-ation-regulated carrier concentration modulation: (g) Downward polarization states in CIPS, and the channel layer is in the electron depletion state; (h) shows light-induced ferroelectric polarization reversal of CIPS. (i) Synaptic transition from STP to LTP enabled by prolonged the duration of light pulse. (j) Potentiation and depression behavior induced by successive optical and negative gate-voltage spike pulses. (k) Simulation of associative learning and extinction by the light pulse and electric pulse. (a and b) Reproduced with permission.[246] Copyright 2023, American Chemical Society. (c–f) Reproduced with permission.[189] Copyright 2024, Wiley-VCH. (g–k) Reproduced with permission.[183] Copyright 2024, Wiley-VCH.

photodetectors that integrate photon capture and information retention within a single device. For example, α-In$_2$Se$_3$ exhibits a bulk photovoltaic effect,[89,91,233] and its photodetectors show polarization-dependent responsivity. In the upward polarization state, the responsivity increases by approximately three orders of magnitude compared to the down-state.[184] Zhang *et al.* proposed an optoelectronic nonvolatile memory based on the ferroelectric properties of α-In$_2$Se$_3$.[233] Gr-In$_2$Se$_3$ devices can operate in volatile (photodetector) or nonvolatile (optical random-access memory, ORAM) modes, depending on the dipole orientations within the α-In$_2$Se$_3$ stack.[246]

In addition to narrow bandgap materials, wide-bandgap 2D ferroelectrics such as CIPS (2.7 eV) has been explored for optoelectronic applications with the aid of light-induced migration of Cu$^+$ ions. Liu *et al.* demonstrated optoelectronic conductance modulation in a CIPS-based device with asymmetric electrodes (Graphene/CIPS/Au) (Fig. 14c).[189] When the applied voltage (± 2 V) is below the ferroelectric coercive voltage of CIPS (± 4 V), current modulation is primarily driven by light-assisted Cu$^+$ ion hopping. The device presents rectification behavior, due to the interfacial Schottky barrier (Fig. 14d). Upon illumination, photogenerated electron–hole pairs are separated by the internal field, triggering a photoconductive response. The resulting current initially spikes, then gradually saturates. Upon cessation of light exposure, a sudden drop followed by slow decay is observed, with the current remaining above baseline (Fig. 14e). This behavior indicates a memory effect. The photocurrent scales linearly with light intensity, affirming that the number of photogenerated carriers is power-dependent. Leveraging this effect, the device mimics synaptic learning and forgetting under optical pulses (Fig. 14f), demonstrating short-term potentiation under weak light and long-term potentiation under prolonged illumination. Furthermore, Shang *et al.*[247] reported a photoelectric synaptic device based on a longitudinal CIPS structure, capable of simulating the basic characteristics of biological visual systems and associative learning behaviors. Owing to its ultrasensitive photodetection properties, the energy consumption per synaptic event is less than 0.36 pJ.

Beyond light-induced Cu$^+$ migration mechanism, light-induced depolarization field mechanism has also been demonstrated. In an all-VdW SnS$_2$/BN/CIPS Fe-FET (Fig. 14g),[183] the device exhibits high-performance memory functionality and supports neuromorphic vision system applications. Initially, CIPS possesses a downward polarization, which gradually reverses under illumination (Fig. 14g and h). This switching is facilitated by the compensation of ferroelectric polarization charges in CIPS by photogenerated carriers in SnS$_2$, which modulate the built-in electric field. By varying light pulse duration (Fig. 14i), frequency, and intensity, the retention time and synaptic weights can be tuned, analogous to the STP-to-LTP transition observed in biological systems. The device also supports photonic potentiation and electrical depression operations (Fig. 14j), with a high on/off current ratio of over 10^5, a long retention time over 10^4 s, stable cyclic endurance of over 350 switching cycles, and 128 multilevel current states. These features enable advanced memory storage and retrieval, while also supporting neuromorphic functions such as retina-like light adaptation and Pavlovian conditioning (Fig. 14k).

4. Challenges and outlooks

In this review, we have systematically examined five primary coupling mechanisms employed in 2D ferroelectric materials for artificial synapse applications: polarization-only, polarization-ion coupling, polarization-carrier coupling, polarization-polarization coupling, and polarization-light stimulation. Section 2 provides a comparative analysis of these coupling mechanisms at the material level, while section 3 focuses on their implementation at the device level, highlighting their distinct physical characteristics and the associated trade-offs in neuromorphic applications. Each coupling mechanism exhibits unique advantages and limitations, making it suitable for specific functional requirements or application-driven goals. A summary of their key features and neuromorphic behaviors is illustrated in Fig. 15.

Devices based on the polarization-only mechanism can be structurally classified into two-terminal and three-terminal synaptic structures. Two-terminal memristors rely on switching internal polarization states or modulating interface potential barriers to emulate synaptic weight variation. Owing to their compact structure, they are well-suited for high-density integration in crossbar arrays. However, they are vulnerable to
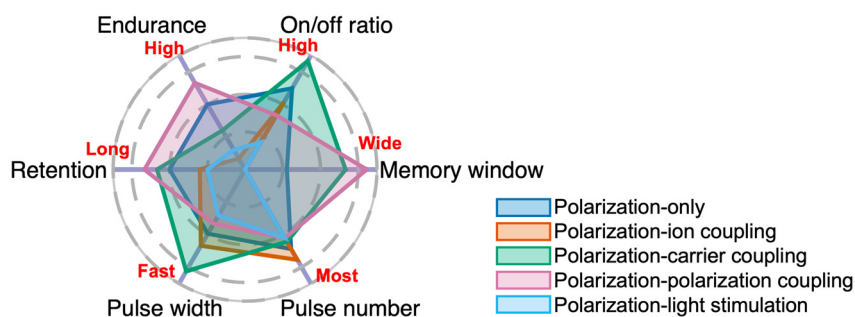

Fig. 15 Schematic illustration of summarized characteristics of 2D FE synaptic device corresponding to each coupling mechanism.

current interference and sneak path issues, which can degrade the accuracy and hinder precise signal transmission and weight updates. Moreover, the stochastic formation of conductive filaments reduces reliability, and the learning function and signal transmission process cannot be realized simultaneously due to the single tunable conducting channel between two electrodes.[3] In contrast, three-terminal synaptic devices overcome these limitations by decoupling the conductance modulation path from the signal transmission path. This separation enhances functional modularity, allows more reliable weight updating, and improves operational stability. For functional layer, employing high-k 2D dielectric (*e.g.* HfO_2, Al_2O_3) in FeFETs may enhance the carrier mobility by suppressing the coulombic impurity scattering effect and preventing the interfacial chemical reaction.[248] While for channel layer, oxide channel materials such as ZnO, IGZO, and In_2O_3 may deal with the reliability concerns in FeFET.[194] Additionally, floating gate (FG) FeFETs that utilize charge trapping and de-trapping in the floating layer to achieve nonvolatile behavior also represent a promising research direction.[3]

Ferroionic neuromorphic devices that couple ionic migration with ferroelectric switching are particularly capable of emulating various neuroplasticity functions, as ion movement within the device closely resembles neurotransmitter dynamics in biological synapses. However, this coupling mechanism often suffers from performance variability and limited data retention due to the high sensitivity of ionic conductivity, leading to reliability issues.[195] Achieving stable resistive switching (RS) remains a significant challenge within this coupling mechanism. To address these issues, electrochemically active electrodes, such as silver (Ag) and copper (Cu), have been introduced to enhance the stability and performance of RS devices based on ionic conduction. Cu electrodes promote a stronger concentration gradient and facilitate faster ion diffusion, enabling more stable RS characteristics with low variation in threshold and hold voltages.[223] Ag electrodes, in contrast, operate based on the formation and rupture of metallic filaments. Devices with higher compliance currents produce thicker and more robust filaments, thereby improving retention.[144] Furthermore, utilizing advanced methods to confine the active region to a 1D channel may mitigate variability issues.[195] Additionally, coupling of ion migration behavior with multiple ferroic orders, such as ferroelectricity and ferromagnetism, could enable novel physical properties,[84,86] opening new avenues for future research.

Polarization-carrier coupling mechanism, realized in FeS-FET, effectively mitigates depolarization effects through mobile charge screening, thereby reducing interfacial charge trapping, gate leakage and short retention times. As a result, these devices demonstrate enhanced non-volatility and low power consumption. Moreover, the coexistence of intercorrelated IP and OOP polarization allows multi-terminal modulation (*via* both drain and gate terminals), supporting more complex operational modes.[34,226] Since ferroelectric semiconductors serve as the channel material in FeS-FETs, the dielectric layer can be independently optimized; for example,

integrating a high-k dielectric enables lower-voltage operation,[227] making this a promising path for practical device design.

Polarization-polarization coupling mechanism benefits from enhanced retention time due to dipole–dipole interactions between stacked ferroelectric layers.[133,176,230,231] However, this mechanism is currently limited by material availability, as it requires ferroelectric semiconductors as channel that possess both switchable polarization and semiconducting properties. Despite some promising examples such as α-In_2Se_3, the number of experimentally verified 2D ferroelectric semiconductors remains limited. Additionally, a major drawback of this coupling mechanism is its typically large hysteresis window (often exceeding 10 V), which poses challenges for low-power operation. Research based on this coupling mechanism is still in its early stage, and future efforts will be needed to address high operating voltage and expand material availability.

Polarization–light stimulation coupling introduces an additional sensory modality that is not present in other mechanisms. This enables the integration of sensing, memory, and computation within a single device, mimicking retina-like functionality found in biological visual systems.[162,183,245] Furthermore, optoelectronic–ferroelectric effects can be explored by synergistically combining light stimulation with other coupling mechanisms, offering new opportunities for multifunctional device design.

Despite the considerable progress, several challenges remain before 2D ferroelectric materials can be adopted in practical neuromorphic hardware. At the material level, issues such as environmental instability, polarization fatigue, and low Curie temperatures limit device reliability and thermal operating range. Scalable growth methods like chemical vapor deposition (CVD) still face difficulties in producing large-scale, uniform, and high-quality films. Promising strategies include alloy engineering, encapsulation, and computationally guided material discovery to identify new 2D ferroelectrics with higher Curie temperatures and improved stability. At the device level, integration into van der Waals heterostructures often suffers from interface defects that trap charges and degrade performance. Achieving CMOS compatibility requires low-temperature fabrication processes and careful mitigation of parasitic capacitance. Additionally, stacking multiple layers introduces strain and thermal mismatch, affecting polarization alignment and retention time. Solutions such as atomic-layer passivation, monolithic stacking on flexible substrates, and the use of solid electrolytes for ferroionic gating may improve device integrity and integration feasibility.[30,63,239]

Functional challenges also remain. Ferroelectric-based synaptic devices often suffer from nonlinear and asymmetric weight updates due to domain wall pinning, which reduces training accuracy.[233,249] The energy consumption of ferroelectric spiking neurons remains substantially higher than biological counterparts. Furthermore, polarization noise in quantum ferroelectric devices limits coherence and stability. Future opportunities lie in the development of moiré ferroelectrics for

fault-tolerant states, light-responsive synapses for ultra-fast plasticity, and analog in-memory computing using multi-domain FeFETs.[137,139,142] Continued interdisciplinary research across materials science, electronics, and neuroscience will be essential to overcome these challenges and fully realize the potential of 2D ferroelectric materials in neuromorphic and quantum technologies.

Conflicts of interest

There are no conflicts to declare.

Data availability

This article is a review and does not contain any original experimental data. All data discussed and analyzed in this work are derived from previously published studies, which are appropriately cited throughout the manuscript. No new data were generated for this review.

Acknowledgements

References

1 M. D. Godfrey, *Ann. Hist. Comput.*, 1993, **15**, 11–21.

2 Y. Zhan, Y. Mei and L. Zheng, *J. Mater. Chem. C*, 2014, **2**, 1220–1232.

3 Q. Zhang, Z. Zhang, C. Li, R. Xu, D. Yang and L. Sun, *Chip*, 2023, **2**, 100059.

4 W. Wang, Y. Meng, W. Wang, Y. Zhang, B. Li, Y. Yan, B. Gao and J. C. Ho, *Mater. Today Electron.*, 2023, **6**, 100080.

5 X. Lin, Y. Li, Y. Lei and Q. Sun, *Int. J. Smart Nano Mater.*, 2024, **15**, 238–259.

6 K. Wang, M. Wang, B. Sun, C. Yang, Z. Cao, T. Wu, K. Gao, H. Ma, W. Yan, H. Wang, L. Fu, X. Li and J. Shao, *Nano Energy*, 2025, **136**, 110698.

7 A. Wali and S. Das, *Adv. Funct. Mater.*, 2024, **34**, 2308129.

8 S. Pazos, K. Zhu, M. A. Villena, O. Alharbi, W. Zheng, Y. Shen, Y. Yuan, Y. Ping and M. Lanza, *Nature*, 2025, **640**, 69–76.

9 A. Gautam and T. Kohno, *Biomimetics*, 2022, **7**, 246.

10 L. Yin, X. Pi and D. Yang, *Chin. Phys. B*, 2020, **29**, 070703.

11 P. A. Merolla, J. V. Arthur, R. Alvarez-Icaza, A. S. Cassidy, J. Sawada, F. Akopyan, B. L. Jackson, N. Imam, C. Guo, Y. Nakamura, B. Brezzo, I. Vo, S. K. Esser, R. Appuswamy, B. Taba, A. Amir, M. D. Flickner, W. P. Risk, R. Manohar and D. S. Modha, *Science*, 2014, **345**, 668–673.

12 M. Davies, N. Srinivasa, T.-H. Lin, G. Chinya, Y. Cao, S. H. Choday, G. Dimou, P. Joshi, N. Imam, S. Jain, Y. Liao, C.-K. Lin, A. Lines, R. Liu, D. Mathaikutty, S. McCoy, A. Paul, J. Tse, G. Venkataramanan, Y.-H. Weng, A. Wild, Y. Yang and H. Wang, *IEEE Micro*, 2018, **38**, 82–99.

13 J. Pei, L. Deng, S. Song, M. Zhao, Y. Zhang, S. Wu, G. Wang, Z. Zou, Z. Wu, W. He, F. Chen, N. Deng, S. Wu, Y. Wang, Y. Wu, Z. Yang, C. Ma, G. Li, W. Han, H. Li, H. Wu, R. Zhao, Y. Xie and L. Shi, *Nature*, 2019, **572**, 106–111.

14 C. Frenkel, M. Lefebvre, J.-D. Legat and D. Bol, *IEEE Trans. Biomed. Circuits Syst.*, 2019, **13**, 145–158.

15 H. Hendy and C. Merkel, *J. Electron Imag.*, 2022, **31**, 010901.

16 S. Furber, *J. Neural Eng.*, 2016, **13**, 051001.

17 M. Davies, A. Wild, G. Orchard, Y. Sandamirskaya, G. A. F. Guerra, P. Joshi, P. Plank and S. R. Risbud, *Proc. IEEE*, 2021, **109**, 911–934.

18 A. Mehonic, D. Ielmini, K. Roy, O. Mutlu, S. Kvatinsky, T. Serrano-Gotarredona, B. Linares-Barranco, S. Spiga, S. Savel'ev, A. G. Balanov, N. Chawla, G. Desoli, G. Malavena, C. M. Compagnoni, Z. Wang, J. J. Yang, S. G. Sarwat, A. Sebastian, T. Mikolajick, S. Slesazeck, B. Noheda, B. Dieny, T.-H. (Alex) Hou, A. Varri, F. Brückerhoff-Plückelmann, W. Pernice, X. Zhang, S. Pazos, M. Lanza, S. Wiefels, R. Dittmann, W. H. Ng, M. Buckwell, H. R. J. Cox, D. J. Mannion, A. J. Kenyon, Y. Lu, Y. Yang, D. Querlioz, L. Hutin, E. Vianello, S. S. Chowdhury, P. Mannocci, Y. Cai, Z. Sun, G. Pedretti, J. P. Strachan, D. Strukov, M. Le Gallo, S. Ambrogio, I. Valov and R. Waser, *APL Mater.*, 2024, **12**, 109201.

19 H. Zhou, S. Li, K.-W. Ang and Y.-W. Zhang, *Nano-Micro Lett.*, 2024, **16**, 121.

20 C. Li, X. Zhang, P. Chen, K. Zhou, J. Yu, G. Wu, D. Xiang, H. Jiang, M. Wang and Q. Liu, *iScience*, 2023, **26**, 106315.

21 Q. Lu, F. Sun, L. Liu, L. Li, Y. Wang, M. Hao, Z. Wang, S. Wang and T. Zhang, *Microsyst. Nanoeng.*, 2020, **6**, 84.

22 Y. Sun, J. Li, S. Li, Y. Jiang, E. Wan, Jiahan Zhang, Y. Shi and L. Pan, *Chip*, 2023, **2**, 100031.

23 G. Cao, P. Meng, J. Chen, H. Liu, R. Bian, C. Zhu, F. Liu and Z. Liu, *Adv. Funct. Mater.*, 2021, **31**, 2005443.

24 Y. Joo, E. Hwang, H. Hong, S. Cho and H. Yang, *Adv. Electrode Mater.*, 2023, **9**, 2300211.

25 A. Velichko and P. Boriskov, *IEEE Trans. Circuits Syst. II: Express Briefs*, 2020, **67**, 3477–3481.

26 J. Liu, Y. Huang, Y. Luo, H. Jim and M. Liam, *Neurocomputing*, 2019, **331**, 473–482.

27 R. Yang, H.-M. Huang, Q.-H. Hong, X.-B. Yin, Z.-H. Tan, T. Shi, Y.-X. Zhou, X.-S. Miao, X.-P. Wang, S.-B. Mi, C.-L. Jia and X. Guo, *Adv. Funct. Mater.*, 2018, **28**, 1704455.

28 W. Ci, P. Wang, W. Xue, H. Yuan and X. Xu, *Adv. Funct. Mater.*, 2024, **34**, 2316360.

29 Y. Kim, J. H. Baek, I. H. Im, D. H. Lee, M. H. Park and H. W. Jang, *ACS Nano*, 2024, **18**, 34531–34571.

30 J. Bi, Y. Li, R. Lu, H. Song and J. Jiang, *J. Semicond.*, 2025, **46**, 021401.

31 K. C. Kwon, J. H. Baek, K. Hong, S. Y. Kim and H. W. Jang, *Nano-Micro Lett.*, 2022, **14**, 58.

32 A. Sebastian, M. Le Gallo, R. Khaddam-Aljameh and E. Eleftheriou, *Nat. Nanotechnol.*, 2020, **15**, 529–544.

33 Hebbian Learning – an overview | ScienceDirect Topics, **https://www.sciencedirect.com/topics/psychology/hebbian-learning**, (accessed April 8, 2025).

34 J. Gao, Y. Zheng, W. Yu, Y. Wang, T. Jin, X. Pan, K. P. Loh and W. Chen, *SmartMat*, 2021, **2**, 88–98.

35 Z. Liu, Y. Wang, Y. Zhang, S. Sun, T. Zhang, Y.-J. Zeng, L. Hu, F. Zhuge, B. Lu, X. Pan and Z. Ye, *Adv. Mater.*, 2025, **37**, 2410783.

36 Z. Wang, X. Zhou, X. Liu, A. Qiu, C. Gao, Y. Yuan, Y. Jing, D. Zhang, W. Li, H. Luo, J. Chu and J. Sun, *Chip*, 2023, **2**, 100044.

37 Z.-D. Luo, S. Zhang, Y. Liu, D. Zhang, X. Gan, J. Seidel, Y. Liu, G. Han, M. Alexe and Y. Hao, *ACS Nano*, 2022, **16**, 3362–3372.

38 J. Liu, W. Han, E. Hong, M. Deng, Z. Li, L. Wu and X. Fang, *Adv. Funct. Mater.*, 2025, 2425350.

39 S. Pazos, K. Zhu, M. A. Villena, O. Alharbi, W. Zheng, Y. Shen, Y. Yuan, Y. Ping and M. Lanza, *Nature*, 2025, **640**, 69–76.

40 H. Hong, X. Chen, W. Cho, H. Y. Yoo, J. Oh, M. Kim, G. Hwang, Y. Yang, L. Sun, Z. Wang and H. Yang, *Adv. Funct. Mater.*, 2025, **35**, 2422321.

41 M. Yan, Q. Zhu, S. Wang, Y. Ren, G. Feng, L. Liu, H. Peng, Y. He, J. Wang, P. Zhou, X. Meng, X. Tang, J. Chu, B. Dkhil, B. Tian and C. Duan, *Adv. Electrode Mater.*, 2021, **7**, 2001276.

42 Y. Huang, L. Wang, F. Zhang, W. Ming, Y. Liu, S. Zhu, Y. Li, W. Wang and C. Li, *ACS Appl. Mater. Interfaces*, 2025, **17**, 40623–40629.

43 J. Chen, C. Zhu, G. Cao, H. Liu, R. Bian, J. Wang, C. Li, J. Chen, Q. Fu, Q. Liu, P. Meng, W. Li, F. Liu and Z. Liu, *Adv. Mater.*, 2022, **34**, 2104676.

44 W. Zhang, B. Gao, J. Tang, P. Yao, S. Yu, M.-F. Chang, H.-J. Yoo, H. Qian and H. Wu, *Nat. Electron.*, 2020, **3**, 371–382.

45 T. Pfeil, A.-C. Scherzer, J. Schemmel and K. Meier, in *The 2013 International Joint Conference on Neural Networks (IJCNN)*, 2013, pp. 1–5.

46 S. Yan, J. Zang, P. Xu, Y. Zhu, G. Li, Q. Chen, Z. Chen, Y. Zhang, M. Tang and X. Zheng, *Sci. China Mater.*, 2023, **66**, 877–894.

47 J. Valasek, *Phys. Rev.*, 1921, **17**, 475–481.

48 L. Ortega-San-Martin, in *Revolution of Perovskite: Synthesis, Properties and Applications*, ed. N. S. Arul and V. D. Nithya, Springer, Singapore, 2020, pp. 1–41.

49 Y. Wang, J. Yan, H. Cheng, N. Chen, P. Yan, F. Yang and J. Ouyang, *Ceram. Int.*, 2019, **45**, 9032–9037.

50 J. Chen, Y.-Q. Zhu, X.-C. Zhao, Z.-H. Wang, K. Zhang, Z. Zhang, M.-Y. Sun, S. Wang, Y. Zhang, L. Han, X. Wu and T.-L. Ren, *Nano Lett.*, 2023, **23**, 10196–10204.

51 J. Du, D. Xie, Q. Zhang, H. Zhong, F. Meng, X. Fu, Q. Sun, H. Ni, T. Li, E. Guo, H. Guo, M. He, C. Wang, L. Gu, X. Xu, G. Zhang, G. Yang, K. Jin and C. Ge, *Nano Energy*, 2021, **89**, 106439.

52 L. D. Namade, A. R. Patil, S. R. Jadhav, T. D. Dongale and K. Y. Rajpure, *Colloids Surf., A*, 2024, **692**, 133902.

53 M.-K. Kim and J.-S. Lee, *Nano Lett.*, 2019, **19**, 2044–2050.

54 H. Xiang, Y. Chien, L. Li, H. Zheng, S. Li, N. T. Duong, Y. Shi and K. Ang, *Adv. Funct. Mater.*, 2023, 2304657.

55 C. Song, D. Kim, S. Lee and H. Kwon, *Adv. Sci.*, 2024, **11**, 2308588.

56 Y. Zeng, Y. Lei, Y. Wang, M. Cheng, L. Liao, X. Wang, J. Ge, Z. Liu, W. Ming, C. Li, S. Xie, J. Li and C. Li, *Small Methods*, 2024, **9**, 2400722.

57 K.-H. Kim, S. Oh, M. M. A. Fiagbenu, J. Zheng, P. Musavigharavi, P. Kumar, N. Trainor, A. Aljarb, Y. Wan, H. M. Kim, K. Katti, S. Song, G. Kim, Z. Tang, J.-H. Fu, M. Hakami, V. Tung, J. M. Redwing, E. A. Stach, R. H. Olsson and D. Jariwala, *Nat. Nanotechnol.*, 2023, **18**, 1044–1050.

58 Y. Wang, L. Tao, R. Guzman, Q. Luo, W. Zhou, Y. Yang, Y. Wei, Y. Liu, P. Jiang, Y. Chen, S. Lv, Y. Ding, W. Wei, T. Gong, Y. Wang, Q. Liu, S. Du and M. Liu, *Science*, 2023, **381**, 558–563.

59 K. Xu, T. Wang, C. Lu, Y. Song, Y. Liu, J. Yu, Y. Liu, Z. Li, J. Meng, H. Zhu, Q.-Q. Sun, D. W. Zhang and L. Chen, *Nano Lett.*, 2024, **24**, 11170–11178.

60 Y. Hu, M. Rabelo, T. Kim, J. Cho, J. Choi, X. Fan and J. Yi, *Trans. Electr. Electron. Mater.*, 2023, **24**, 271–278.

61 H. Xu, F. Sun, E. Li, W. Guo, L. Hua, R. Wang, W. Li, J. Chu, W. Liu, J. Luo and Z. Sun, *Adv. Mater.*, 2025, **37**, 2414339.

62 S. Oh, H. Hwang and I. K. Yoo, *APL Mater.*, 2019, **7**, 091109.

63 W. Jie, X. Fei, L. Zheng-Dong, T. Dongxin, G. X. Tao, Z. Dawei, C. Zhufei, X. Yinshui, L. Yan and H. Genquan, *Sci. China Inf. Sci.*, 2025, **68**, 152401.

64 Z. Dang, F. Guo, H. Duan, Q. Zhao, Y. Fu, W. Jie, K. Jin and J. Hao, *Nano Lett.*, 2023, **23**, 6752–6759.

65 Z. Dang, F. Guo, Z. Wang, W. Jie, K. Jin, Y. Chai and J. Hao, *ACS Nano*, 2024, **18**, 27727–27737.

66 M. Liu, T. Liao, Z. Sun, Y. Gu and L. Kou, *Phys. Chem. Chem. Phys.*, 2021, **23**, 21376–21384.

67 S. B. Desai, S. R. Madhvapathy, A. B. Sachid, J. P. Llinas, Q. Wang, G. H. Ahn, G. Pitner, M. J. Kim, J. Bokor, C. Hu, H.-S. P. Wong and A. Javey, *Science*, 2016, **354**, 99–102.

68 L. Liu, Y. Chen, L. Chen, B. Xie, G. Li, L. Kong, Q. Tao, Z. Li, X. Yang, Z. Lu, L. Ma, D. Lu, X. Yang and Y. Liu, *Nat. Commun.*, 2024, **15**, 165.

69 Y. Wang, S. Sarkar, H. Yan and M. Chhowalla, *Nat. Electron.*, 2024, **7**, 638–645.

70 D. Zeng, Z. Zhang, Z. Xue, M. Zhang, P. K. Chu, Y. Mei, Z. Tian and Z. Di, *Nature*, 2024, **632**, 788–794.

71 B. Radisavljevic, A. Radenovic, J. Brivio, V. Giacometti and A. Kis, *Nat. Nanotechnol.*, 2011, **6**, 147–150.

72 Z. Yin, H. Li, H. Li, L. Jiang, Y. Shi, Y. Sun, G. Lu, Q. Zhang, X. Chen and H. Zhang, *ACS Nano*, 2012, **6**, 74–80.

73 K. S. Novoselov, D. Jiang, F. Schedin, T. J. Booth, V. V. Khotkevich, S. V. Morozov and A. K. Geim, *Proc. Natl. Acad. Sci. U. S. A.*, 2005, **102**, 10451–10453.

74 A. Belianinov, Q. He, A. Dziaugys, P. Maksymovych, E. Eliseev, A. Borisevich, A. Morozovska, J. Banys, Y. Vysochanskii and S. V. Kalinin, *Nano Lett.*, 2015, **15**, 3808–3814.

75 F. Liu, L. You, K. L. Seyler, X. Li, P. Yu, J. Lin, X. Wang, J. Zhou, H. Wang, H. He, S. T. Pantelides, W. Zhou, P. Sharma, X. Xu, P. M. Ajayan, J. Wang and Z. Liu, *Nat. Commun.*, 2016, **7**, 12357.

76 M. Chyasnavichyus, M. A. Susner, A. V. Ievlev, E. A. Eliseev, S. V. Kalinin, N. Balke, A. N. Morozovska, M. A. McGuire and P. Maksymovych, *Appl. Phys. Lett.*, 2016, **109**, 172901.

77 S. M. Neumayer, E. A. Eliseev, M. A. Susner, A. Tselev, B. J. Rodriguez, J. A. Brehm, S. T. Pantelides, G. Panchapakesan, S. Jesse, S. V. Kalinin, M. A. McGuire, A. N. Morozovska, P. Maksymovych and N. Balke, *Phys. Rev. Mater.*, 2019, **3**, 024401.

78 L. Chen, Y. Li, C. Li, H. Wang, Z. Han, H. Ma, G. Yuan, L. Lin, Z. Yan, X. Jiang and J.-M. Liu, *AIP Adv.*, 2019, **9**, 115211.

79 L. You, Y. Zhang, S. Zhou, A. Chaturvedi, S. A. Morris, F. Liu, L. Chang, D. Ichinose, H. Funakubo, W. Hu, T. Wu, Z. Liu, S. Dong and J. Wang, *Sci. Adv.*, 2019, **5**, 3780.

80 Z.-Z. Sun, W. Xun, L. Jiang, J.-L. Zhong and Y.-Z. Wu, *J. Phys. D: Appl. Phys.*, 2019, **52**, 465302.

81 Y. Lai, Z. Song, Y. Wan, M. Xue, C. Wang, Y. Ye, L. Dai, Z. Zhang, W. Yang, H. Du and J. Yang, *Nanoscale*, 2019, **11**, 5163–5170.

82 R.-R. Ma, D.-D. Xu, Q.-L. Zhong, C.-R. Zhong, R. Huang, P.-H. Xiang, N. Zhong and C.-G. Duan, *Adv. Mater. Interfaces*, 2022, **9**, 2101769.

83 W. F. Io, S.-Y. Pang, L. W. Wong, Y. Zhao, R. Ding, J. Mao, Y. Zhao, F. Guo, S. Yuan, J. Zhao, J. Yi and J. Hao, *Nat. Commun.*, 2023, **14**, 7304.

84 Y. Ma, Y. Yan, L. Luo, S. Pazos, C. Zhang, X. Lv, M. Chen, C. Liu, Y. Wang, A. Chen, Y. Li, D. Zheng, R. Lin, H. Algaidi, M. Sun, J. Z. Liu, S. Tu, H. N. Alshareef, C. Gong, M. Lanza, F. Xue and X. Zhang, *Nat. Commun.*, 2023, **14**, 7891.

85 G. Dushaq, S. Serunjogi, S. R. Tamalampudi and M. Rasras, *Light: Sci. Appl.*, 2024, **13**, 92.

86 Q. Hu, Y. Huang, Y. Wang, S. Ding, M. Zhang, C. Hua, L. Li, X. Xu, J. Yang, S. Yuan, K. Watanabe, T. Taniguchi, Y. Lu, C. Jin, D. Wang and Y. Zheng, *Nat. Commun.*, 2024, **15**, 3029.

87 H. Chen, Y. Long, S. Zhang, K. Liu, M. Chen, J. Zhao, M. Si and L. Wang, *Adv. Mater.*, 2025, **37**, 2419125.

88 Y. Ma, M. Chen, F. Aguirre, Y. Yan, S. Pazos, C. Liu, H. Wang, T. Yang, B. Wang, C. Gong, K. Liu, J. Z. Liu, M. Lanza, F. Xue and X. Zhang, *Nano Lett.*, 2025, **25**, 2528–2537.

89 M. Lin, D. Wu, Y. Zhou, W. Huang, W. Jiang, W. Zheng, S. Zhao, C. Jin, Y. Guo, H. Peng and Z. Liu, *J. Am. Chem. Soc.*, 2013, **135**, 13274–13277.

90 W. Ding, J. Zhu, Z. Wang, Y. Gao, D. Xiao, Y. Gu, Z. Zhang and W. Zhu, *Nat. Commun.*, 2017, **8**, 14956.

91 Y. Zhou, D. Wu, Y. Zhu, Y. Cho, Q. He, X. Yang, K. Herrera, Z. Chu, Y. Han, M. C. Downer, H. Peng and K. Lai, *Nano Lett.*, 2017, **17**, 5508–5513.

92 C. Cui, W.-J. Hu, X. Yan, C. Addiego, W. Gao, Y. Wang, Z. Wang, L. Li, Y. Cheng, P. Li, X. Zhang, H. N. Alshareef, T. Wu, W. Zhu, X. Pan and L.-J. Li, *Nano Lett.*, 2018, **18**, 1253–1258.

93 J. Xiao, H. Zhu, Y. Wang, W. Feng, Y. Hu, A. Dasgupta, Y. Han, Y. Wang, D. A. Muller, L. W. Martin, P. Hu and X. Zhang, *Phys. Rev. Lett.*, 2018, **120**, 227601.

94 F. Xue, W. Hu, K. Lee, L. Lu, J. Zhang, H. Tang, A. Han, W. Hsu, S. Tu, W. Chang, C. Lien, J. He, Z. Zhang, L. Li and X. Zhang, *Adv. Funct. Mater.*, 2018, **28**, 1803738.

95 C.-M. Yang, T.-C. Chen, D. Verma, L.-J. Li, B. Liu, W.-H. Chang and C.-S. Lai, *Adv. Funct. Mater.*, 2020, **30**, 2001598.

96 W. Wang, Y. Meng, Y. Zhang, Z. Zhang, W. Wang, Z. Lai, P. Xie, D. Li, D. Chen, Q. Quan, D. Yin, C. Liu, Z. Yang, S. Yip and J. C. Ho, *Adv. Mater.*, 2023, **35**, 2210854.

97 U. Khan, R. Xu, A. Nairan, M. Han, X. Wang, L. Kong, J. Gao and L. Tang, *Adv. Funct. Mater.*, 2024, **34**, 2315522.

98 X. Ren, X. He, X. Li, Y. Li, F. Gao, J. Zhang and P. Hu, *Adv. Opt. Mater.*, 2024, **12**, 2302852.

99 L. Tang, L. Dang, M. Han, S. Li, U. Khan, W. Chen, Z. Cai, L. Kong, Q. Wu, B. Liu, Q. Zhang, R. Xu and X. Ma, *Adv. Funct. Mater.*, 2024, **34**, 2405898.

100 Y. Li, L. Wang, Y. Ouyang, D. Li, Y. Yan, K. Dai, L. Shang, J. Zhang, L. Zhu, Y. Li and Z. Hu, *Mater. Today*, 2025, **83**, 12–23.

101 K. Chang, J. Liu, H. Lin, N. Wang, K. Zhao, A. Zhang, F. Jin, Y. Zhong, X. Hu, W. Duan, Q. Zhang, L. Fu, Q.-K. Xue, X. Chen and S.-H. Ji, *Science*, 2016, **353**, 274–278.

102 Y. Bao, P. Song, Y. Liu, Z. Chen, M. Zhu, I. Abdelwahab, J. Su, W. Fu, X. Chi, W. Yu, W. Liu, X. Zhao, Q.-H. Xu, M. Yang and K. P. Loh, *Nano Lett.*, 2019, **19**, 5109–5117.

103 H. Q. Yang, X. Y. Wang, H. Wu, B. Zhang, D. D. Xie, Y. J. Chen, X. Lu, X. D. Han, L. Miao and X. Y. Zhou, *J. Mater. Chem. C*, 2019, **7**, 3351–3359.

104 N. Higashitarumizu, H. Kawamoto, C.-J. Lee, B.-H. Lin, F.-H. Chu, I. Yonemori, T. Nishimura, K. Wakabayashi, W.-H. Chang and K. Nagashio, *Nat. Commun.*, 2020, **11**, 2428.

105 K. C. Kwon, Y. Zhang, L. Wang, W. Yu, X. Wang, I.-H. Park, H. S. Choi, T. Ma, Z. Zhu, B. Tian, C. Su and K. P. Loh, *ACS Nano*, 2020, **14**, 7628–7638.

106 L. Sun, Z. Wang, J. Jiang, Y. Kim, B. Joo, S. Zheng, S. Lee, W. J. Yu, B.-S. Kong and H. Yang, *Sci. Adv.*, 2021, 7, 1455.

107 Z. Fei, W. Zhao, T. A. Palomaki, B. Sun, M. K. Miller, Z. Zhao, J. Yan, X. Xu and D. H. Cobden, *Nature*, 2018, 560, 336–339.

108 Q. Yang, M. Wu and J. Li, *J. Phys. Chem. Lett.*, 2018, 9, 7160–7164.

109 P. Sharma, F.-X. Xiang, D.-F. Shao, D. Zhang, E. Y. Tsymbal, A. R. Hamilton and J. Seidel, *Sci. Adv.*, 2019, 5, 5080.

110 S. Yuan, X. Luo, H. L. Chan, C. Xiao, Y. Dai, M. Xie and J. Hao, *Nat. Commun.*, 2019, 10, 1775.

111 J. W. Park, Y. S. Jung, S. H. Park, H.-J. Choi and Y. S. Cho, *Adv. Opt. Mater.*, 2022, 10, 2200898.

112 M. Wu, *ACS Nano*, 2021, 15, 9229–9237.

113 L. Qi, S. Ruan and Y. Zeng, *Adv. Mater.*, 2021, 33, 2005098.

114 Z. Wang, X. Zhou, X. Liu, A. Qiu, C. Gao, Y. Yuan, Y. Jing, D. Zhang, W. Li, H. Luo, J. Chu and J. Sun, *Chip*, 2023, 2, 100044.

115 Y. Liu, M. Lian, W. Chen and H. Chen, *Int. J. Extreme Manuf.*, 2024, 6, 022008.

116 E. Yu, G. K. Kumar, U. Saxena and K. Roy, *Sci. Rep.*, 2024, 14, 9426.

117 A. J. Arnold, A. Razavieh, J. R. Nasr, D. S. Schulman, C. M. Eichfeld and S. Das, *ACS Nano*, 2017, 11, 3110–3118.

118 H. Lee, V. K. Sangwan, W. A. G. Rojas, H. Bergeron, H. Y. Jeong, J. Yuan, K. Su and M. C. Hersam, *Adv. Funct. Mater.*, 2020, 30, 2003683.

119 J. Yuan, S. E. Liu, A. Shylendra, W. A. G. Rojas, S. Guo, H. Bergeron, S. Li, H.-S. Lee, S. Nasrin, V. K. Sangwan, A. R. Trivedi and M. C. Hersam, *Nano Lett.*, 2021, 21, 6432–6440.

120 W. Huh, S. Jang, J. Y. Lee, D. Lee, D. Lee, J. M. Lee, H. Park, J. C. Kim, H. Y. Jeong, G. Wang and C. Lee, *Adv. Mater.*, 2018, 30, 1801447.

121 Z. Guan, H. Hu, X. Shen, P. Xiang, N. Zhong, J. Chu and C. Duan, *Adv. Electron. Mater.*, 2020, 6, 1900818.

122 S. Lin, G. Zhang, Q. Lai, J. Fu, W. Zhu and H. Zeng, *Adv. Funct. Mater.*, 2023, 33, 2304139.

123 C. Chen, Y. Zhou, L. Tong, Y. Pang and J. Xu, *Adv. Mater.*, 2024, 37, 2400332.

124 H. Wang, Y. Wen, H. Zeng, Z. Xiong, Y. Tu, H. Zhu, R. Cheng, L. Yin, J. Jiang, B. Zhai, C. Liu, C. Shan and J. He, *Adv. Mater.*, 2024, 2305044.

125 L. Niu, F. Liu, Q. Zeng, X. Zhu, Y. Wang, P. Yu, J. Shi, J. Lin, J. Zhou, Q. Fu, W. Zhou, T. Yu, X. Liu and Z. Liu, *Nano Energy*, 2019, 58, 596–603.

126 K. Cho, S. Lee, R. Kalaivanan, R. Sankar, K.-Y. Choi and S. Park, *Adv. Funct. Mater.*, 2022, 32, 2204214.

127 S. Xie, A. Dey, W. Yan, Z. R. Kudrynskyi, N. Balakrishnan, O. Makarovsky, Z. D. Kovalyuk, E. G. Castanon, O. Kolosov, K. Wang and A. Patanè, *2D Mater.*, 2021, 8, 045020.

128 T. Ghosh, M. Samanta, A. Vasdev, K. Dolui, J. Ghatak, T. Das, G. Sheet and K. Biswas, *Nano Lett.*, 2019, 19, 5703–5709.

129 X. Wang, C. Zhu, Y. Deng, R. Duan, J. Chen, Q. Zeng, J. Zhou, Q. Fu, L. You, S. Liu, J. H. Edgar, P. Yu and Z. Liu, *Nat. Commun.*, 2021, 12, 1109.

130 N. Higashitarumizu, H. Kawamoto, C.-J. Lee, B.-H. Lin, F.-H. Chu, I. Yonemori, T. Nishimura, K. Wakabayashi, W.-H. Chang and K. Nagashio, *Nat. Commun.*, 2020, 11, 2428.

131 U. Khan, R. Xu, A. Nairan, M. Han, X. Wang, L. Kong, J. Gao and L. Tang, *Adv. Funct. Mater.*, 2024, 34, 2315522.

132 Y. Li, J. Fu, X. Mao, C. Chen, H. Liu, M. Gong and H. Zeng, *Nat. Commun.*, 2021, 12, 5896.

133 S. Park, D. Lee, J. Kang, H. Choi and J.-H. Park, *Nat. Commun.*, 2023, 14, 6778.

134 W. Wang, W. Luo, S. Zhang, C. Zeng, F. Xie, C. Deng, G. Wang and G. Peng, *Nanomaterials*, 2024, 14, 1638.

135 I. Zulfiqar, M. A. Khan, S. Gul, N. U. Hassan, M. A. Rehman, M. A. Basit, H. M. W. Khalil, M. Ouladsmane, S. Rehman and M. F. Khan, *Phys. B*, 2023, 669, 415313.

136 J. A. Brehm, S. M. Neumayer, L. Tao, A. O'Hara, M. Chyasnavichus, M. A. Susner, M. A. McGuire, S. V. Kalinin, S. Jesse, P. Ganesh, S. T. Pantelides, P. Maksymovych and N. Balke, *Nat. Mater.*, 2020, 19, 43–48.

137 Y. Wang, Z. Zeng, Z. Tian, C. Li, K. Braun, L. Huang, Y. Li, X. Luo, J. Yi, G. Wu, G. Liu, D. Li, Y. Zhou, M. Chen, X. Wang and A. Pan, *Adv. Mater.*, 2024, 36, 2410696.

138 X. Li, B. Qin, Y. Wang, Y. Xi, Z. Huang, M. Zhao, Y. Peng, Z. Chen, Z. Pan, J. Zhu, C. Cui, R. Yang, W. Yang, S. Meng, D. Shi, X. Bai, C. Liu, N. Li, J. Tang, K. Liu, L. Du and G. Zhang, *Nat. Commun.*, 2024, 15, 10921.

139 S. Du, W. Yang, H. Gao, W. Dong, B. Xu, K. Watanabe, T. Taniguchi, J. Zhao, F. Zheng, J. Zhou and S. Zheng, *Adv. Mater.*, 2024, 36, 2404177.

140 R. Bian, R. He, E. Pan, Z. Li, G. Cao, P. Meng, J. Chen, Q. Liu, Z. Zhong, W. Li and F. Liu, *Science*, 2024, 385, 57–62.

141 W. Li, X. Zhang, J. Yang, S. Zhou, C. Song, P. Cheng, Y.-Q. Zhang, B. Feng, Z. Wang, Y. Lu, K. Wu and L. Chen, *Nat. Commun.*, 2023, 14, 2757.

142 G. Sánchez-Santolino, V. Rouco, S. Puebla, H. Aramberri, V. Zamora, M. Cabero, F. A. Cuellar, C. Munuera, F. Mompean, M. Garcia-Hernandez, A. Castellanos-Gomez, J. Íñiguez, C. Leon and J. Santamaria, *Nature*, 2024, 626, 529–534.

143 J. Gou, H. Bai, X. Zhang, Y. L. Huang, S. Duan, A. Ariando, S. A. Yang, L. Chen, Y. Lu and A. T. S. Wee, *Nature*, 2023, 617, 67–72.

144 Y. Liu, Y. Wu, B. Wang, H. Chen, D. Yi, K. Liu, C.-W. Nan and J. Ma, *Nano Res.*, 2023, 16, 10191–10197.

145 W. Ming, B. Huang, S. Zheng, Y. Bai, J. Wang, J. Wang and J. Li, *Sci. Adv.*, 2022, 8, 1232.

146 C. Chen, H. Liu, Q. Lai, X. Mao, J. Fu, Z. Fu and H. Zeng, *Nano Lett.*, 2022, 22, 3275–3282.

147 B. Li, S. Li, H. Wang, L. Chen, L. Liu, X. Feng, Y. Li, J. Chen, X. Gong and K. Ang, *Adv. Electrode Mater.*, 2020, 6, 2000760.

148 Z. Zhao, K. Xu, H. Ryu and W. Zhu, *ACS Appl. Mater. Interfaces*, 2020, **12**, 51820–51826.

149 Y. Wu, N. T. Duong, Y. Chien, S. Liu and K. Ang, *Adv. Electrode Mater.*, 2024, **10**, 2300481.

150 D. Zhang, Z.-D. Luo, Y. Yao, P. Schoenherr, C. Sha, Y. Pan, P. Sharma, M. Alexe and J. Seidel, *Nano Lett.*, 2021, **21**, 995–1002.

151 S. Zhou, L. You, H. Zhou, Y. Pu, Z. Gui and J. Wang, *Front. Phys.*, 2021, **16**, 13301.

152 J. Zhou, A. Chen, Y. Zhang, D. Pu, B. Qiao, J. Hu, H. Li, S. Zhong, R. Zhao, F. Xue, Y. Xu, K. P. Loh, H. Wang and B. Yu, *Adv. Mater.*, 2023, **35**, 2302419.

153 S. Zhou, L. You, A. Chaturvedi, S. A. Morris, J. S. Herrin, N. Zhang, A. Abdelsamie, Y. Hu, J. Chen, Y. Zhou, S. Dong and J. Wang, *Mater. Horiz.*, 2020, **7**, 263.

154 M. A. Susner, M. Chyasnavichyus, A. A. Puretzky, Q. He, B. S. Conner, Y. Ren, D. A. Cullen, P. Ganesh, D. Shin, H. Demir, J. W. McMurray, A. Y. Borisevich, P. Maksymovych and M. A. McGuire, *ACS Nano*, 2017, **11**, 7060–7073.

155 S. Wang, L. Liu, L. Gan, H. Chen, X. Hou, Y. Ding, S. Ma, D. W. Zhang and P. Zhou, *Nat. Commun.*, 2021, **12**, 53.

156 H. Shi, M. Li, A. S. Nia, M. Wang, S. Park, Z. Zhang, M. R. Lohe, S. Yang and X. Feng, *Adv. Mater.*, 2020, **32**, 1907244.

157 A. K. Saha, M. Si, P. D. Ye and S. K. Gupta, *Appl. Phys. Lett.*, 2020, **117**, 183504.

158 X. Chen, K. Xu, T. Qin, Y. Wang, Q. Xiong and H. Liu, *Nanoscale*, 2025, **17**, 5005–5011.

159 L. Wang, H. Chen, M. Chen, Y. Long, K. Liu and K. P. Loh, *Adv. Funct. Mater.*, 2024, **34**, 2316583.

160 Q. He, B. Jiang, J. Ma, W. Chen, X. Luo and Y. Zheng, *Small Methods*, 2024, **9**, 2401549.

161 K. Liu, T. Zhang, B. Dang, L. Bao, L. Xu, C. Cheng, Z. Yang, R. Huang and Y. Yang, *Nat. Electron.*, 2022, **5**, 761–773.

162 W. Ci, W. Xue, P. Wang, W. Yin, X. Wang, L. Shi, P. Zhou and X. Xu, *Adv. Funct. Mater.*, 2024, **34**, 2305822.

163 C. Zhao, Z. Gao, Z. Hong, H. Guo, Z. Cheng, Y. Li, L. Shang, L. Zhu, J. Zhang and Z. Hu, *Adv. Sci.*, 2025, **12**, 2413808.

164 Y. Wang, Y. Cai, S. Li, X. Zhan, R. Cheng, Z. Wang, J. He and F. Wang, *Small*, 2025, **21**, 2409922.

165 J. Zhou, A. Chen, Y. Zhang, X. Zhang, J. Chai, J. Hu, H. Li, Y. Xu, X. Liu, N. Tan, F. Xue and B. Yu, *Nano Lett.*, 2024, **24**, 14892–14900.

166 J. Zeng, G. Feng, G. Wu, J. Liu, Q. Zhao, H. Wang, S. Wu, X. Wang, Y. Chen, S. Han, B. Tian, C. Duan, T. Lin, J. Ge, H. Shen, X. Meng, J. Chu and J. Wang, *Adv. Funct. Mater.*, 2024, **34**, 2313010.

167 K. Si, Y. Zhao, P. Zhang, X. Wang, Q. He, J. Wei, B. Li, Y. Wang, A. Cao, Z. Hu, P. Tang, F. Ding and Y. Gong, *Nat. Commun.*, 2024, **15**, 7471.

168 C. Zhang, B. Zheng, G. Wu, X. Liu, J. Wu, C. Yao, Y. Wang, Z. Tang, Y. Chen, L. Fang, L. Huang, D. Li, S. Li and A. Pan, *Nano Res.*, 2024, **17**, 1856–1863.

169 J. Liao, W. Wen, J. Wu, Y. Zhou, S. Hussain, H. Hu, J. Li, A. Liaqat, H. Zhu, L. Jiao, Q. Zheng and L. Xie, *ACS Nano*, 2023, **17**, 6095–6102.

170 J. Jiang, L. Xu, C. Qiu and L.-M. Peng, *Nature*, 2023, **616**, 470–475.

171 M. Lin, L. Liao, D. Wu, Y. Huang, J. Wu, L. Wang, W. Xu, Y. Zhang, J. Song, Y. Zhang and C. Li, *Small*, 2025, **21**, 2500026.

172 G. Jin and L. He, *npj Comput. Mater.*, 2024, **10**, 1–6.

173 J. Kang, H. Lee, A. Tunga, X. Xu, Y. Lin, Z. Zhao, H. Ryu, C.-C. Tsai, T. Taniguchi, K. Watanabe, S. Rakheja and W. Zhu, *ACS Nano*, 2025, **19**, 12948–12959.

174 Z. Zhang, S. Huo, Q. Tian, F. Meng, Z. Yang, Y. Ma, Y. Wang, Y. Xie, X. Hu, W. Gao, E. Wu and C. Pan, *Adv. Funct. Mater.*, 2025, **35**, 2424728.

175 A. Jindal, A. Saha, Z. Li, T. Taniguchi, K. Watanabe, J. C. Hone, T. Birol, R. M. Fernandes, C. R. Dean, A. N. Pasupathy and D. A. Rhodes, *Nature*, 2023, **613**, 48–52.

176 Y. Li, Y. Yang, H. Zhao, H. Duan, C. Yang, T. Min and T. Li, *Nano Lett.*, 2025, **25**, 1680–1688.

177 H. Jiao, X. Wang, S. Wu, Y. Chen, J. Chu and J. Wang, *Appl. Phys. Rev.*, 2023, **10**, 011310.

178 W. Park, J. H. Yang, C. G. Kang, Y. G. Lee, H. J. Hwang, C. Cho, S. K. Lim, S. C. Kang, W.-K. Hong, S. K. Lee, S. Lee and B. H. Lee, *Nanotechnology*, 2013, **24**, 475501.

179 Y. Lee, J. Park, S. Cho, Y.-E. Shin, H. Lee, J. Kim, J. Myoung, S. Cho, S. Kang, C. Baig and H. Ko, *ACS Nano*, 2018, **12**, 4045–4054.

180 J. Pang, T. Duan, M. Liao, L. Jiang, Y. Zhou, Q. Yang, J. Liao and J. Jiang, *npj Flexible Electron.*, 2025, **9**, 7.

181 H. Shao, Y. Ji, R. Wang, J. Liu, Y. Li, B. Liu, W. Li, Y. Xie, L. Xie, J. C. Ho, W. Huang and H. Ling, *Nano Energy*, 2024, **130**, 110133.

182 X. Liu, D. Wang, W. Chen, Y. Kang, S. Fang, Y. Luo, D. Luo, H. Yu, H. Zhang, K. Liang, L. Fu, B. S. Ooi, S. Liu and H. Sun, *Nat. Commun.*, 2024, **15**, 7671.

183 P. Wang, J. Li, W. Xue, W. Ci, F. Jiang, L. Shi, F. Zhou, P. Zhou and X. Xu, *Adv. Sci.*, 2024, **11**, 2305679.

184 C. Jia, S. Wu, J. Fan, C. Luo, M. Fan, M. Li, L. He, Y. Yang and H. Zhang, *ACS Nano*, 2023, **17**, 6534–6544.

185 T. Li, A. Lipatov, H. Lu, H. Lee, J.-W. Lee, E. Torun, L. Wirtz, C.-B. Eom, J. Íñiguez, A. Sinitskii and A. Gruverman, *Nat. Commun.*, 2018, **9**, 3344.

186 H. Tan, G. Castro, J. Lyu, P. Loza-Alvarez, F. Sánchez, J. Fontcuberta and I. Fina, *Mater. Horiz.*, 2022, **9**, 2345–2352.

187 J. Yu, S. Yang, W. Ming, Y. Zhang, S. Xu, B. Huang, Q. Wang and J. Li, *Nano Lett.*, 2025, **25**, 3471–3478.

188 R.-R. Ma, D.-D. Xu, Z. Guan, X. Deng, F. Yue, R. Huang, Y. Chen, N. Zhong, P.-H. Xiang and C.-G. Duan, *Appl. Phys. Lett.*, 2020, **117**, 131102.

189 Y. Liu, Y. Wu, H. Han, Y. Wang, R. Peng, K. Liu, D. Yi, C. Nan and J. Ma, *Adv. Funct. Mater.*, 2024, **34**, 2306945.

190 Z. Wen and D. Wu, *Adv. Mater.*, 2020, **32**, 1904123.

191 H. Sun, Z. Luo, C. Liu, C. Ma, Z. Wang, Y. Yin and X. Li, *J. Materiomics*, 2022, **8**, 144–149.

192 R. Athle and M. Borg, *Adv. Intell. Syst.*, 2024, **6**, 2300554.

193 H. Ryu, H. Wu, F. Rao and W. Zhu, *Sci. Rep.*, 2019, **9**, 20383.

194 J. Ajayan, P. Mohankumar, D. Nirmal, L. M. I. L. Joseph, S. Bhattacharya, S. Sreejith, S. Kollem, S. Rebelli, S. Tayal and B. Mounika, *Mater. Today Commun.*, 2023, **35**, 105591.

195 N. K. Upadhyay, H. Jiang, Z. Wang, S. Asapu, Q. Xia and J. J. Yang, *Adv. Mater. Technol.*, 2019, **4**, 1800589.

196 J. Y. Kim, M.-J. Choi and H. W. Jang, *APL Mater.*, 2021, **9**, 021102.

197 J. Niu, D. Kim, J. Li, J. Lyu, Y. Lee and S. Lee, *ACS Nano*, 2025, **19**, 5493–5502.

198 M.-K. Kim, I.-J. Kim and J.-S. Lee, *Sci. Adv.*, 2022, **8**, 8537.

199 M.-Y. Cha, H. Liu, T.-Y. Wang, L. Chen, H. Zhu, L. Ji, Q.-Q. Sun and D. W. Zhang, *AIP Adv.*, 2020, **10**, 065107.

200 F. Yang, H. K. Ng, X. Ju, W. Cai, J. Cao, D. Chi, A. Suwardi, G. Hu, Z. Ni, X. R. Wang, J. Lu and J. Wu, *Adv. Funct. Mater.*, 2024, **34**, 2310438.

201 A. N. Morozovska, E. A. Eliseev, I. S. Vorotiahin, M. V. Silibin, S. V. Kalinin and N. V. Morozovsky, *Acta Mater.*, 2018, **160**, 57–71.

202 C.-Y. Chan, K.-Y. Chen, H.-K. Peng and Y.-H. Wu, in 2020 IEEE Symposium on VLSI Technology, 2020, pp. 1–2.

203 M. Benkhelifa, S. Thomann, K. Ni and H. Amrouch, *npj Unconv. Comput.*, 2025, **2**, 16.

204 H.-K. Peng, C.-Y. Chan, K.-Y. Chen and Y.-H. Wu, *Appl. Phys. Lett.*, 2021, **118**, 103503.

205 F. Mo, Y. Tagawa, C. Jin, M. Ahn, T. Saraya, T. Hiramoto and M. Kobayashi, *IEEE J. Electron Devices Soc.*, 2020, **8**, 717–723.

206 N. Thoti and Y. Li, *Nanotechnology*, 2022, **33**, 055201.

207 H. Mulaosmanovic, U. Schroeder, T. Mikolajick and S. Slesazeck, in *Ferroelectric-Gate Field Effect Transistor Memories: Device Physics and Applications*, ed. B.-E. Park, H. Ishiwara, M. Okuyama, S. Sakai and S.-M. Yoon, Springer, Singapore, 2020, pp. 97–108.

208 K.-T. Chen, H.-Y. Chen, C.-Y. Liao, G.-Y. Siang, C. Lo, M.-H. Liao, K.-S. Li, S. T. Chang and M. H. Lee, *IEEE Electron Device Lett.*, 2019, **40**, 399–402.

209 C.-Y. Liao, C.-Y. Lin, Z.-X. Lee, K.-Y. Hsiang, Z.-F. Lou, V. P.-H. Hu and M.-H. Lee, *Appl. Phys. Lett.*, 2022, **121**, 252902.

210 Y. Y. Illarionov, G. Rzepa, M. Waltl, T. Knobloch, A. Grill, M. M. Furchi, T. Mueller and T. Grasser, *2D Mater.*, 2016, **3**, 035004.

211 S. Kim, H. Yoo and J. Choi, *Sensors*, 2023, **23**, 2265.

212 I. Katsouras, D. Zhao, M.-J. Spijkman, M. Li, P. W. M. Blom, D. M. D. Leeuw and K. Asadi, *Sci. Rep.*, 2015, **5**, 12094.

213 Y. Sun, D. Xie, R. Dai, M. Sun, W. Li and T. Ren, *Curr. Appl. Phys.*, 2018, **18**, 324–328.

214 X. Gao, Q. Chen, Q. Qin, L. Li, M. Liu, D. Hao, J. Li, J. Li, Z. Wang and Z. Chen, *Nano Res.*, 2024, **17**, 1886–1892.

215 M. Park, J. Y. Yang, M. J. Yeom, B. Bae, Y. Baek, G. Yoo and K. Lee, *Sci. Adv.*, 2023, **9**, 9889.

216 L. Zhao, Y. Liang, J. Ma, Z. Pan, X. Liu, M. Yang, Y. Sun, W. Gao, B. Li, J. Li and N. Huo, *Adv. Funct. Mater.*, 2023, **33**, 2306708.

217 P. Singh, S. Baek, H. H. Yoo, J. Niu, J.-H. Park and S. Lee, *ACS Nano*, 2022, **16**, 5418–5426.

218 X. Jiang, X. Hu, J. Bian, K. Zhang, L. Chen, H. Zhu, Q. Sun and D. W. Zhang, *ACS Appl. Electron. Mater.*, 2021, **3**, 4711–4717.

219 J. Wu, H.-Y. Chen, N. Yang, J. Cao, X. Yan, F. Liu, Q. Sun, X. Ling, J. Guo and H. Wang, *Nat. Electron.*, 2020, **3**, 466–472.

220 J. Y. Yang, M. Park, M. J. Yeom, Y. Baek, S. C. Yoon, Y. J. Jeong, S. Y. Oh, K. Lee and G. Yoo, *ACS Nano*, 2023, **17**, 7695–7704.

221 Y. Zhang, L. Wang, H. Chen, T. Ma, X. Lu and K. P. Loh, *Adv. Electrode Mater.*, 2021, **7**, 2100609.

222 Y. Sun, R. Zhang, C. Teng, J. Tan, Z. Zhang, S. Li, J. Wang, S. Zhao, W. Chen, B. Liu and H.-M. Cheng, *Mater. Today*, 2023, **66**, 9–16.

223 Z. Zhong, S. Wu, X. Li, Z. Wang, Q. Yang, B. Huang, Y. Chen, X. Wang, T. Lin, H. Shen, X. Meng, M. Wang, W. Shi, J. Wang, J. Chu and H. Huang, *ACS Nano*, 2023, **17**, 12563–12572.

224 X. Cheng, Z. Zhong, Y. Zhuang, W. Wang, Q. Yang, X. Li, W. Shi, X. Meng, Y. Cao, J. Wang, J. Chu and H. Huang, *Adv. Funct. Mater.*, 2025, 2504017.

225 Y.-R. Jeon, D. Kim, C. Biswas, N. D. Ignacio, P. Carmichael, S. Feng, K. Lai, D.-H. Kim and D. Akinwande, *Adv. Mater.*, 2025, **37**, 2413178.

226 Y. Chen, D. Li, H. Ren, Y. Tang, K. Liang, Y. Wang, F. Li, C. Song, J. Guan, Z. Chen, X. Lu, G. Xu, W. Li, S. Liu and B. Zhu, *Small*, 2022, **18**, 2203611.

227 N. Mohta, A. Rao, N. Remesh, R. Muralidharan and D. N. Nath, *RSC Adv.*, 2021, **11**, 36901–36912.

228 L. Wang, X. Wang, Y. Zhang, R. Li, T. Ma, K. Leng, Z. Chen, I. Abdelwahab and K. P. Loh, *Adv. Funct. Mater.*, 2020, **30**, 2004609.

229 M. Si, A. K. Saha, S. Gao, G. Qiu, J. Qin, Y. Duan, J. Jian, C. Niu, H. Wang, W. Wu, S. K. Gupta and P. D. Ye, *Nat. Electron.*, 2019, **2**, 580–586.

230 S. Baek, H. H. Yoo, J. H. Ju, P. Sriboriboon, P. Singh, J. Niu, J. Park, C. Shin, Y. Kim and S. Lee, *Adv. Sci.*, 2022, **9**, 2200566.

231 J. Niu, S. Jeon, D. Kim, S. Baek, H. H. Yoo, J. Li, J.-S. Park, Y. Lee and S. Lee, *InfoMat*, 2024, **6**, 12490.

232 M. Soliman, K. Maity, A. Gloppe, A. Mahmoudi, A. Ouerghi, B. Doudin, B. Kundys and J.-F. Dayen, *ACS Appl. Mater. Interfaces*, 2023, **15**, 15732–15744.

233 F. Xue, X. He, W. Liu, D. Periyanagounder, C. Zhang, M. Chen, C. Lin, L. Luo, E. Yengel, V. Tung, T. D. Anthopoulos, L. Li, J. He and X. Zhang, *Adv. Funct. Mater.*, 2020, **30**, 2004206.

234 H. Quan, D. Meng, X. Ma and C. Qiu, *ACS Appl. Mater. Interfaces*, 2023, **15**, 45076–45082.

235 W. Li, Y. Guo, Z. Luo, S. Wu, B. Han, W. Hu, L. You, K. Watanabe, T. Taniguchi, T. Alava, J. Chen, P. Gao, X. Li, Z. Wei, L. Wang, Y. Liu, C. Zhao, X. Zhan, Z. V. Han and H. Wang, *Adv. Mater.*, 2023, **35**, 2208266.

236 Y. Wang, W. Li, Y. Guo, X. Huang, Z. Luo, S. Wu, H. Wang, J. Chen, X. Li, X. Zhan and H. Wang, *J. Mater. Sci. Technol.*, 2022, **128**, 239–244.

237 K. Yang, S. Wang, T. Han and H. Liu, *Nanomaterials*, 2021, **11**, 1971.

238 W. Huang, F. Wang, L. Yin, R. Cheng, Z. Wang, M. G. Sendeku, J. Wang, N. Li, Y. Yao and J. He, *Adv. Mater.*, 2020, **32**, 1908040.

239 X. Wang, P. Yu, Z. Lei, C. Zhu, X. Cao, F. Liu, L. You, Q. Zeng, Y. Deng, C. Zhu, J. Zhou, Q. Fu, J. Wang, Y. Huang and Z. Liu, *Nat. Commun.*, 2019, **10**, 3037.

240 D. Wang, Y. Zhang, J. Wang, C. Luo, M. Li, W. Shuai, R. Tao, Z. Fan, D. Chen, M. Zeng, J. Y. Dai, X. B. Lu and J.-M. Liu, *J. Mater. Sci. Technol.*, 2022, **104**, 1–7.

241 W. Sun, B. Gao, M. Chi, Q. Xia, J. J. Yang, H. Qian and H. Wu, *Nat. Commun.*, 2019, **10**, 3453.

242 J. Wang, Y. Ren, Z. Yang, Q. Lv, Y. Zhang, M. Zhang, T. Zhao, D. Gu, F. Liu, B. Tang, W. Yang and Z. Lin, *Adv. Sci.*, 2024, **11**, 2309538.

243 Y. Jang, Y. Jeong, D. P. Pham and J. Yi, *Trans. Electr. Electron. Mater.*, 2024, **25**, 393–399.

244 F. Guo, W. F. Io, Z. Dang, R. Ding, S.-Y. Pang, Y. Zhao and J. Hao, *Mater. Horiz.*, 2023, **10**, 3719–3728.

245 P. Xie, X. Chen, Z. Zeng, W. Wang, Y. Meng, Z. Lai, Q. Quan, D. Li, W. Wang, X. Bu, S. Tsang, S. Yip, J. Sun and J. C. Ho, *Adv. Funct. Mater.*, 2023, **33**, 2209091.

246 S. Mukherjee, D. Dutta, A. Ghosh and E. Koren, *ACS Nano*, 2023, **17**, 22287–22298.

247 Z. Shang, L. Liu, G. Wang, H. Xu, Y. Cui, J. Deng, Z. Lou, Y. Yan, J. Deng, S.-T. Han, T. Zhai, X. Wang, L. Wang and X. Wang, *ACS Nano*, 2024, **18**, 30530–30539.

248 C. Zhou and Y. Chai, *Adv. Electron. Mater.*, 2017, **3**, 1600400.

249 L. Liu, D. Wang, D. Wang, Y. Sun, H. Lin, X. Gong, Y. Zhang, R. Tang, Z. Mai, Z. Hou, Y. Yang, P. Li, L. Wang, Q. Luo, L. Li, G. Xing and M. Liu, *Nat. Commun.*, 2024, **15**, 4534.